Title

Building a Benchtop Prototype Latent Heat Storage System and Performing First-Order Sensitivity Analysis on Thermal Storage Container Parameters to Maintain Al-Si at 577°C for 32 hours

Author

Paudyal, Anshu

Publication Date

2024

Building a Benchtop Prototype Latent Heat Storage System and Performing First-Order Sensitivity Analysis on Thermal Storage Container Parameters to Maintain Al-Si at 577°C for 32 hours

By

ANSHU PAUDYAL
THESIS

Submitted in partial satisfaction of the requirements for the degree of

MASTER OF SCIENCE

in

Electrical and Computer Engineering

in the

OFFICE OF GRADUATE STUDIES

of the

UNIVERSITY OF CALIFORNIA

DAVIS

Approved:

Jerry M. Woodall, Chair

Majdi Abou Najm, Co-Chair

Hooman Rashtian

Committee in Charge

2024

ABSTRACT

BUILDING A BENCHTOP PROTOTYPE LATENT HEAT STORAGE SYSTEM AND PERFORMING FIRST-ORDER SENSITIVITY ANALYSIS ON THERMAL STORAGE CONTAINER PARAMETERS TO MAINTAIN AL-SI AT 577°C FOR 32 HOURS

APRIL 2024

ANSHU PAUDYAL
B.E., M.S., UNIVERSITY OF CALIFORNIA, DAVIS
Directed by: Jerry M. Woodall and Majdi Abou Najm

As the world moves towards a more sustainable future with increased deployment of renewable energy sources, thermal energy storage offers a solution to the intermittent issue of the primary source of renewable energy: the sun. Latent heat storage, a type of thermal energy storage system, utilizes a phase change material to absorb and release thermal energy. In this study, we aim to achieve two objectives. Firstly, we seek to test a small-scale prototype of a latent heat system using Al-Si as a phase change material (PCM). Secondly, we aim to optimize parameters of the thermal energy storage tank for a household in the United States to sustain eutectic Al-Si at its phase change temperature (577 °C) for 24-30 hrs. We explore various tank structure layer configurations and manipulate parameters to achieve optimal values for target parameters such as heat loss and time. To build the small-scale latent heat system, we assessed the subsystems within the prototype design to ensure their compatibility with the overall system. The design was initiated by research done by a previous lab member, and the necessary equipment was procured and tested for viability. To optimize the parameters for storage tank, we employed a sensitivity analysis approach. This involved defining both the input and target parameters, observing how the adjustments to the input parameters impacted the target variables, and devising strategies to achieve the desired target values. We also explored the practical feasibility of implementing these manipulations. Through the experiments, thermoelectric generator test highlighted issues with imperfect contact and lower output efficiency, necessitating higher quantities of TEG for more energy conversion. Additionally, 304 stainless steel was deemed unsuitable for long-term containment of molten Al-Si due to prolonged exposure. Moreover, the heating setup was inefficient due to thermal inconsistencies and non-uniform heating. While the demonstration of the benchtop LHB wasn't entirely successful, it provided valuable insights into the small-scale latent heat system using Al-Si as a phase change material and emphasized the need for extensive preliminary research in this interdisciplinary field. Secondly, the theoretical analysis provides insights into optimizing thermal storage tank parameters to sustain phase change material at 577 °C for 24-32 hours. Temperature across the layers, material thickness, and emissivity are the key parameters affecting the system's performance. Case 1, without vacuum layer, achieves desired outcome with adjustment of few parameters, notably the thickness of kaowool insulation. On the other hand, Case 3 required manipulation of numerous parameters but fails to offer significant advantage over Case 1 . Temperature of the alumina in contact with the molten Al-Si (which is known as T_alsi in this study), temperature before vacuum (which is the temperature of the surface before vacuum), emissivity, and thickness of kaowool was observed to have significant effect on the target parameters. Notably, the system greatly depends on the low value of emissivity (0.0045) which is 85% smaller than emissivity of polished silver (0.03) which is one of the lowest values of emissivity at operation temperature practically possible in the ideal case. Therefore, achieving an extremely low emissivity value is currently unattainable. In addition, the mechanical structure needed to maintain vacuum layer complicates the system, increasing system cost and complexity. Thermal energy storage is a multidimensional and multidisciplinary framework and while our

study does not propose novel solutions to the challenges of thermal energy storage, both experimental and theoretical methodologies offer insights into the fundamental hurdles facing such systems. In comparison to Case 3, Case 1 emerges as a more feasible option for optimizing thermal storage tanks employing Al-Si as phase change materials, presenting a practical solution with fewer complexities.

To pure joy experienced while working

on physics problems all night…

ACKNOWLEDGEMENT

My professors and teachers have played a huge role in my learning journey. Without their inspiration, support, and courage, I would not be the person I am today.

Firstly, I would like to express my gratitude to Professor Jerry M. Woodall and Majdi Abou Najm for providing me with the opportunity and for investing in and directing me through my master's project. Without their unwavering support and patience, I would not have been able to complete this journey. Thank you for allowing me the time I needed to work on my thesis.

I also want to acknowledge the contributions of Adrian, Krishna, Joel, and Kirsten for their assistance in the lab at the beginning of the project. Additionally, I am grateful to Professor Bryan M. Jenkins for helping me clarify my conceptual dilemmas. I appreciate the time and effort you dedicated to helping me understand my conceptual errors.

Professor Hooman Rashtian, who initially wrote me a letter of recommendation for my master's program and is now serving as a member of my thesis committee. I am grateful for his dedication to teaching.

Professor William Putnam, who also wrote me a letter of recommendation and provided encouragement during my initial master's journey.

Professors Andre Knoesen and James Nelson, with whom I worked at the UC Davis winery before embarking on the latent heat battery project, for their invaluable guidance in my growth as an engineering student. I am also grateful for all the people at UC Davis that have guided me in this journey.

David Newton, my physics professor at De Anza College, for igniting my passion for science and learning.

I am grateful to Ronald Francis, Shannon Hassett, and Danny Tran for their exceptional teaching. They have been instrumental in shaping my academic journey.

My parents, for always leading by example and teaching me the value of diligence and honest hard work. I am grateful to my little sister for filling my life with laughter.

To my friends, who have supported, tolerated, encouraged, and loved me through my toughest times, I am immensely thankful. I also extend my gratitude to my extended family and family friends, who have always held me in their best wishes.

Finally, Kimberly-Susan Taisacan, whose friendship has made this whole journey more bearable. Thank you for all the laughter and for accepting me with all my flaws.

Table of Contents

LIST OF TABLES

LIST OF FIGURES

LIST OF GRAPHS

LIST OF ABBERVIATION & SYMBOLS

BN	Boron Nitride
CSP	Concentrated Solar Plant
HTF	Heat Transfer Fluid
ID	Inner Diameter
LHS	Latent Heat System
OD	Outer Radius
PCM	Phase Change Material
PCT	Phase Change Temperature
SEM	Scanning Electron Microscopy
TES	Thermal Energy Storage
TEG	Thermoelectric Generator
Al-Si	Aluminum-Silicon
Mg	Magnesium
Zn	Zinc
Al	Aluminum
Si	Silicon
Cu	Copper
CO_2	Carbon Dioxide
$MgO\text{-}Zr_2O_3$	Magnesium Zirconia
$MgCl_2$	Magnesium Chloride
KCl	Potassium Chloride
NaCl	Sodium Chloride

Na_2Co_3	Sodium Carbonate
Al_2O_3	Aluminum Oxide

Units:

kg	Kilogram
K	Kelvin
°C	Degree Celsius
J	Joules
g	gram
cm^3	cubic centimeter
V	Voltage
W	Watts
kWh	Kilowatt-hour
Amp	Ampere
W/m-K	Watt per meter-Kelvin
min/cycle	minutes per cycle
µm	micro-meter
°C/min	Degree Celsius per minute
kW_e	Kilo-Watt electric energy
oz.	ounce

CHAPTER 1: INTRODUCTION

Heat accounts for half of the world’s total final energy consumption, with most of this energy being used in buildings for space and water heating, as well as in various industrial processes such as iron and steel, cement, chemicals, and food processing. The primary sources of heat for these applications are non-renewable sources like fossil fuels and very little renewable sources like solar and wind energy. As the world shifts towards sustainable energy for net zero emissions, it is extremely important to make sure that our energy comes from renewable sources. The main renewable source of energy is solar energy; however, the intermittent nature of this source is a huge disadvantage as it is only available during daylight hours and is sensitive to weather conditions. To replace the existing non-renewable energy sources with renewable sources like solar and wind energy it should be able to provide consistent power reliably to meet the energy demand. Storage and backup systems can be used to meet the demand in the absence of intermittent sources and compensate for its variability.

Thermal energy storage (TES) systems store energy in the form of heat. There are three types of TES: sensible, latent, and thermochemical storage [1]. Sensible thermal energy storage technologies which store energy by changing the temperature of the material without changing the phase have been tested and implemented since 1985 [4]. In recent years, there are studies to replace sensible heat with latent heat systems. Latent heat storage (LHS) involves absorbing and releasing thermal energy during the phase change of a material [2]. Latent heat storage has high storage density and is isothermal in nature compared to sensible heat storage [26]. Therefore, there is ongoing research on finding more efficient and reliable systems with latent heat storage to replace the existing sensible heat storage system. A latent heat storage system consists of four main components: the phase change material (PCM) storage tank, referred to as latent heat battery (LHB) in this report, as well as the power input system, heat exchanger, and energy converter. The power input system will provide input to the LHB, where the power comes from renewable energy sources like the sun. The LHB's role is to store and release energy during the phase change process. Heat exchangers facilitate the transfer the heat within the system, while energy converters transform thermal energy to electrical energy for end users.

1.1 Literature Review

In recent years, there has been a lot of research in finding better materials and systems for thermal storage. In this section, I will review recent research on thermal storage material, storage tank's structural material, and small scale LHS systems. This review should provide comprehensive groundwork to further the study in the field.

1.1.1 Thermal Storage materials

Gokon et al. [29] examined the compatibility of different Al-Si alloy composition as high temperature thermal storage material with graphite-carbon encapsulation under vacuum conditions. They evaluated thermal stability, temperature performance, and oxidation after 20 heating and cooling cycles. Compared to Na_2Co_3, Al-25wt%Si alloy demonstrated several benefits, such as high latent heat capacity, controlled thermal expansion, good repeatability, and no adverse reactions with the graphite crucible. However, it exhibited reaction with stainless steel crucible and showed susceptibility to oxidation.

Wang et al. [31] also studied five Al-Si samples and concluded that there was no large amount of coarse crystalline silicon with no phase segregation even after one thousand times of thermal cycling. The latent heat decreased from 499.2 J/g to 493.4 J/g after one thousand times of thermal cycling, but the melting point of the Al-Si stayed at 580°C even after one thousand thermal cycling. Specific heat also remained unchanged even after one thousand thermal cycles. Thermal diffusivity of Al-Si alloy increased first and then decreased with the increasing of the number of thermal cycle time over the whole temperature range. The highest thermal diffusivity is observed in Al-Si eutectic sample after five hundred thermal cycles. Density also only changed from 2.62 g/cm^3 at 0 cycle to 2.63 g/cm^3 after one thousand cycles. The thermal conductivity increased first and then decreased with the increasing of alloy thermal cycling, however it remained as high as 182 W/m-K at 500°C after one thousand times thermal cycling which is adequate for fast charging and discharging which are crucial for TES application. This study showed that Al-Si alloy as a suitable candidate as phase change material for TES application because the melting point and latent heat is almost no change after more than one thousand cycle and the thermal conductivity is also within adequate level needed for fast charging and discharging application.

Fukahori et al. [34] analyzed Al-Si alloys with varying Si content (0-25% wt.) and found that eutectic composition of Al-Si were superior candidates compared to conventional molten salts as PCMs.

Fernández et al. [32] explores the use of metal and metal alloys as phase change materials (PCMs) for high-temperature thermal storage applications. Among the studied materials, the eutectic alloy Al-12wt%Si, stood out as a strongest candidate for PCM due to its high heat of fusion (560 J/g), high thermal conductivity (160 W/m-K), and stable properties through multiple heating and cooling cycles.

Eutectic metal alloy Mg-51%Zn [32], ternary eutectic alloy Al (60 wt.%)-34Mg-6Zn [32], and ternary eutectic Al-Cu-Si [38] were also suggested as other candidates for PCM offering advantages in terms of thermal diffusivity, heat capacity, energy density, lower melting point, and thermal reliability, although some of them are expensive compared to eutectic Al-Si alloy.

[33],[35], and [36] offer a comprehensive resource for high-temperature PCMs. [33] identifies cost-effective PCMs with a melting range of 500°C to 700°C. [35] provides a solid foundation for theoretical research in the field, while [36] compiles a detailed list of high-temperature PCMs, including their properties. Based on existing research, eutectic Al-Si is suggested as the promising candidate as phase change material for latent heat system, provided there is a reliable storage tank. These studies serve as an excellent starting point for further investigation in the field of thermal storage materials.

1.1.2 Storage tank structure material

Although, their suitability for the operating temperature range for thermal storage tank structural materials, both iron and stainless-steel experienced dissolution and reaction, along with formation of several reaction layers and precipitates [34][37][38] when exposed to molten Al-Si based alloys.

The corrosion tests conducted by Fukahori et al. [34] on Al-Si alloys, varying Si wt.%, revealed that Al_2O_3, AlH, and Si3N4 demonstrated high corrosion resistance to molten Al-Si alloys. Rawson et al. [38] verified alumina, aluminum nitride, silicon nitride as high corrosion resistance to Al-12wt%Si alloys. Furthermore, in a study by Dindi et al. [37], an Al-Si alloy was subjected to a Boron-Nitride-based coating on stainless steel, which demonstrated its effectiveness in corrosion prevention. The coating was effective for corrosion prevention and stable after 720 successive melting and solidification cycles. The cycle time is 44 min/cycle with heating and cooling rate 4.2 °C/min. However, in this laboratory-scale research, a minor ~3µm-wide crack was observed in the coating after its application to the crucible. The effectiveness of the coating also depends on deposition techniques. Rawson et al. [38] made similar observations for stainless steel coated with Boron Nitride (BN). They suggested that the tiny cracks observed after the thermal cycling might have existed before the experiment, forming as the wet coating dried on the metal surface. Rea et al. [18] and [19] applied stabilized magnesium zirconia (MgO-Zr_2O_3) coating on the inner wall of the heat pipes and the storage tank. However, the coating failed which led to steel tank dissolution and caused leakage of PCM. It was concluded that plasma sprayed ceramic coating, specifically MgO-Zr_2O_3 only provided corrosion resistance for the duration of the experiment but may not be a suitable long-term solution to for reliable containment.

Despite extensive research conducted to identify appropriate storage tank structure material and corrosion rate, there appears to be a lack of analysis regarding how these findings apply to commercial-scale systems. Existing literature suggests that graphite and alumina are optimal candidates for storage tank structure materials for Al-Si alloys, however there is a gap addressing how these materials may perform in commercial application.

1.1.3 Small Scale Latent Heat System

Rea et al. [18] studied the first ever small-scale TES prototype that used eutectic Al-Si as a PCM. Heat pipes were employed for efficient heat transfer, a valved thermosyphon was used to regulate the heat flow out of the thermal storage system, and a Stirling engine was employed for the conversion of heat to electricity. This prototype utilized 100 kg of eutectic Al-Si as a storage material, sodium as heat transfer fluid (HTF), and was tested over an 11-day simulated operation. The system achieved a maximum efficiency of 18.5% in converting stored heat to electricity, with a peak power output exceeding $1kW_e$. The study also included temperature measurements at 12 separate locations within the PCM, demonstrating that temperatures throughout the experiment remained within 25 degrees Celsius of the PCM's melting temperature. Furthermore, stable temperature distribution within the PCM was observed. These consistent PCM temperatures indicate a high exergy efficiency of the storage system, attributed to the excellent thermal conductivity of Al-Si and the effective thermal conductivity of sodium heat pipes. Rea et al. [19] also did similar investigation using thermoelectric generator (TEG) to convert heat to electricity concluding that the thermal energy storage system was able to receive and distribute heat with small temperature gradients (< 5°C) throughout the thermal storage tank. Considering the temperature drop between the subsystems, a majority of the temperature drop, ~525 °C, occurred across the TEGs.

1.1.4 Important conclusion from post-commercialization study

Araújo et al. [39] evaluated the thermal loss and storage efficiency of a sensible heat storage tank while considering the impact of climatic conditions, loading levels, and operating temperatures. Results validated against data from Solar Two and Andasol I solar plant showed a 4.55% difference for hot tank heat losses and a 4.82% difference for cold tank heat losses. The storage efficiency was minimally affected by climatic conditions but significantly influenced by operating temperature, with a 10.78% efficiency at 300°C and 89.42% at 600°C. Additionally, tank loading level has a substantial impact, with a 37.35% difference between loaded and unloaded tanks. The study revealed that the storage tank is minimally affected by climate changes, while loading level and operating temperature play significant roles in determining heat loss.

Prieto et al. [40] assessed the performance of tank material (carbon steel, stainless steel) exposed to molten salt in a demo plant for thermal storage operating at 400°C. The hot tank experienced breakaway corrosion due to CO_2 production during preheating. The key takeaway

from this study is the importance of considering chemical reactions that can take place within the tank and the atmosphere it creates, as well as the calculation of corrosion rates. Additionally, the study compared the corrosion resistance of different stainless-steel types. Among the stainless-steel types tested, namely A304L, A316L, and A347, all demonstrated similar resistance to corrosion, with corrosion rates remaining below 1um/year under all tested conditions. While this conclusion was not initially apparent during the testing of the storage material with the storage tank structure material, it was observed to be significant in commercial-scale applications.
Gong et al. [41] assessed the suitability of two steel materials, Ferritic-martensitic steel (P91) and 304 stainless-steel (SS304), for the structure material of a cold tank used in thermal energy using $MgCl_2$-KCl-NaCl molten chloride salt. Corrosion experiments were conducted at 500°C for 1400 hours. The results indicated that P91 exhibits lower corrosion rates, consistently measuring less than 15 µm/year, whereas SS304 displayed more significant corrosion with a rate of 394 µm/year. P91 is recommended to as a favorable option for the cold tank due to its corrosion resistance, cost-effectiveness, and high-temperature mechanical properties, making it suitable for thermal energy storage applications using molten chloride salts.

The post-commercialization study's findings offer valuable insight into areas that require improvement or modification for enhanced thermal energy storage. Related results also provide essential considerations when employing Al-Si as a PCM. Alniamat et al. [42] provides further overview on TES and outlines essential considerations for solar power plants. While it primarily focuses on molten salt-based thermal fluids, the principles discussed are applicable to various phase change materials.

CHAPTER 2: BENCHTOP THERMAL STORAGE SYSTEM

The purpose of a benchtop latent heat system is to demonstrate a small-scale thermal energy storage using eutectic Al-Si alloy and to validate the possibility of power generation with appropriate setup. This section describes experiments that were carried out to achieve this goal. Subsystem testing was performed to check the functionality and compatibility of the materials before putting them all together. Previously, the students of the lab had put forth a theoretical set up for the latent heat system. The current experiments build upon these initial ideas, incorporating several revisions and adjustments.

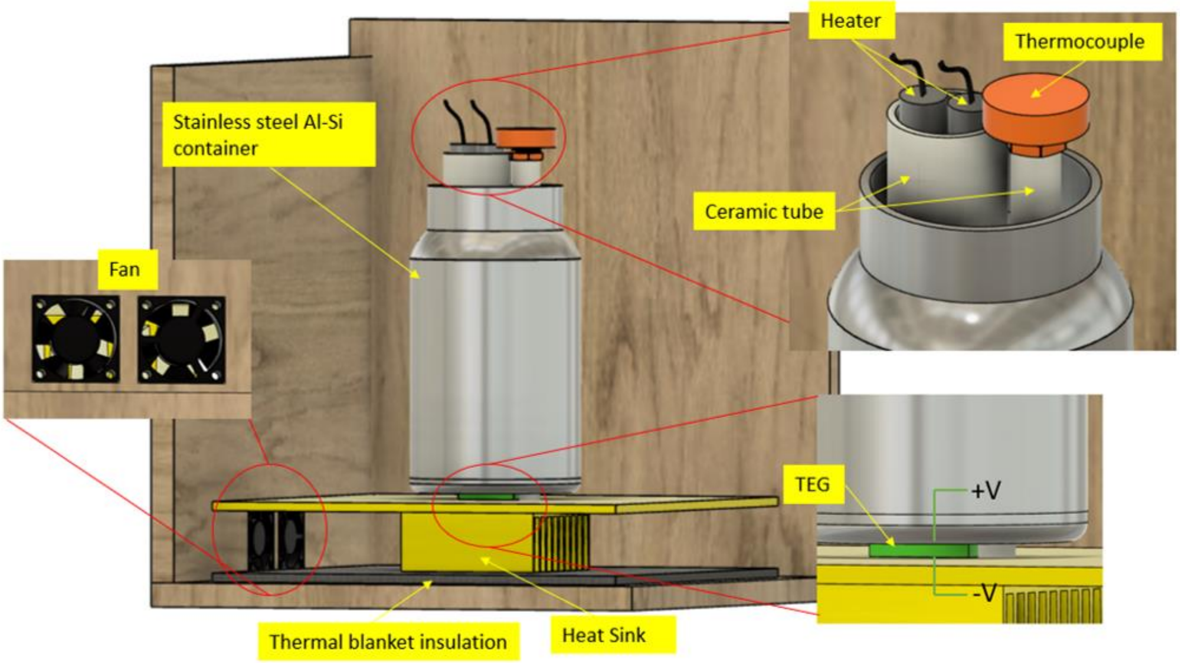

Figure 1: Intended 3D model of the mechanical setup.

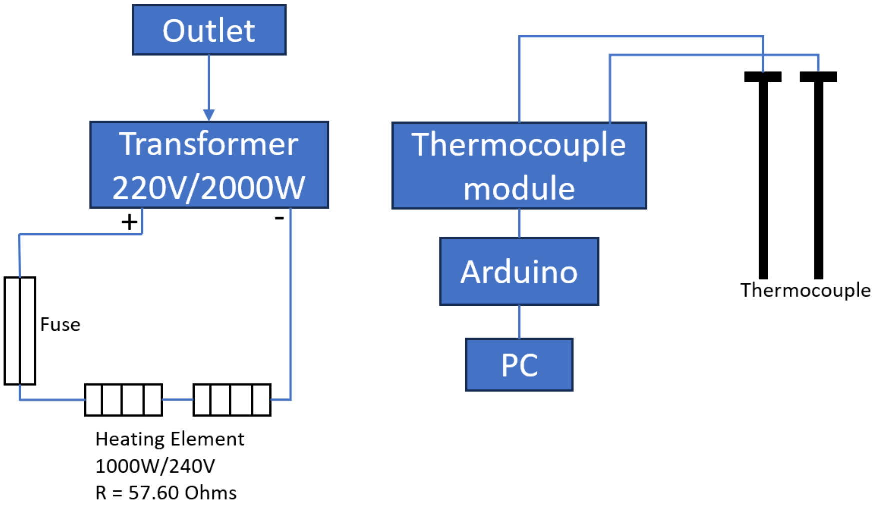

Figure 2: Shows the electrical circuitry in the benchtop system.

2.1 Experiments

In this section, we explore the experiments conducted to assess the viability and feasibility of various benchtop LHS subsystems.

2.1.1 Thermoelectric Generator (TEG) Testing

Thermoelectric generators (TEG) are solid state devices that produce electrical voltage when a temperature difference exists between the bottom and the top plate. We used this device to convert thermal energy into electrical energy. The TEG employed for our application was purchased from TECTEG MFR. and has the efficiency of 12% to 14% when subjected to temperature difference of 425°C to 550°C without a fixed side for hot or cold temperatures. This testing was done to see the maximum achievable voltage output from the TEG under various cooling system conditions.

2.1.1.1 Test 1:

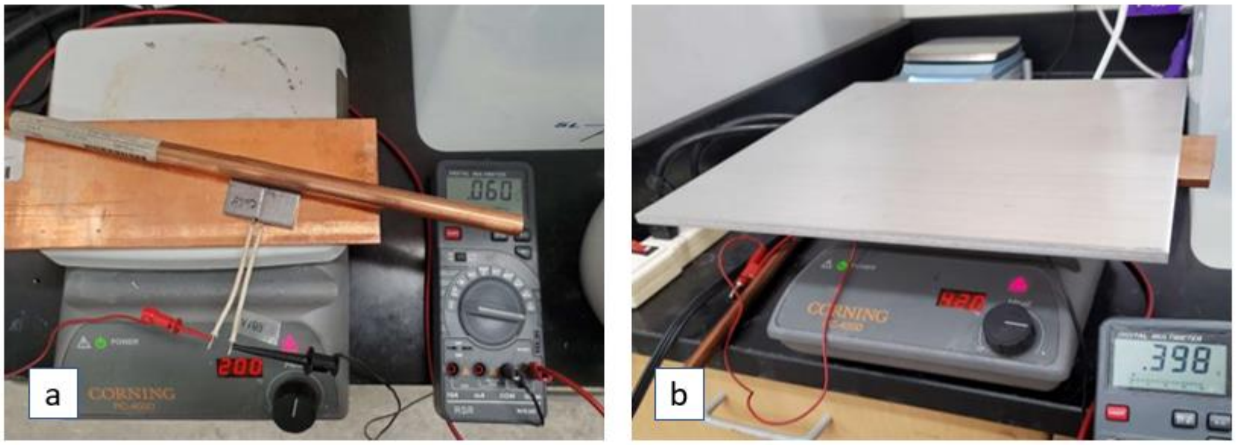

Figure 3:In (a), the TEG placed on the copper slab yields a voltage of 0.060V at a heating plate temperature of 200°C. In (b), with the heating plate temperature increased to 420°C, placing TEG directly on the plate, along with in aluminum heatsink, results in voltage output of 0.398V. The increased pressure and the surface area of aluminum plate enhance heat dissipation on the colder side of the TEG, leading to larger temperature difference between the plates, hence a higher voltage.

2.1.1.2 Test 2:

Figure 4: Shows the experimental set up where room temperature water is used as heat transfer fluid. The heating plate is employed to set hot temperature on one side of the TEG, while the other side is cooled using water heat exchanger. The voltage output of the TEG is measured using the voltmeter. The ring stand holding Al-Si filled cup is used to secure the heat sink in position, preventing it from shaking due to motor's force.

Table 1: Shows the appropriate temperature of the heating plate and heat sink with resulted voltage output.

Steady state time (minutes)	Set temperature of heating plate (°C)	Heat sink temperature (°C)	ΔT (°C)	Voltage @ multimeter (V)
-	100	25	75	0.033
-	155	26	129	0.070
10	400	30	370	0.257
20	400	32	368	0.265
17	550	51	499	0.543

Table 1 illustrates the relationship between the temperature difference (ΔT) across the hot and cold plates of the TEG and the corresponding output voltage. The "Steady State Time" column indicates the duration during which the heating plate remained at the respective temperature before voltage measurement was taken.

2.1.1.3 Test 3:

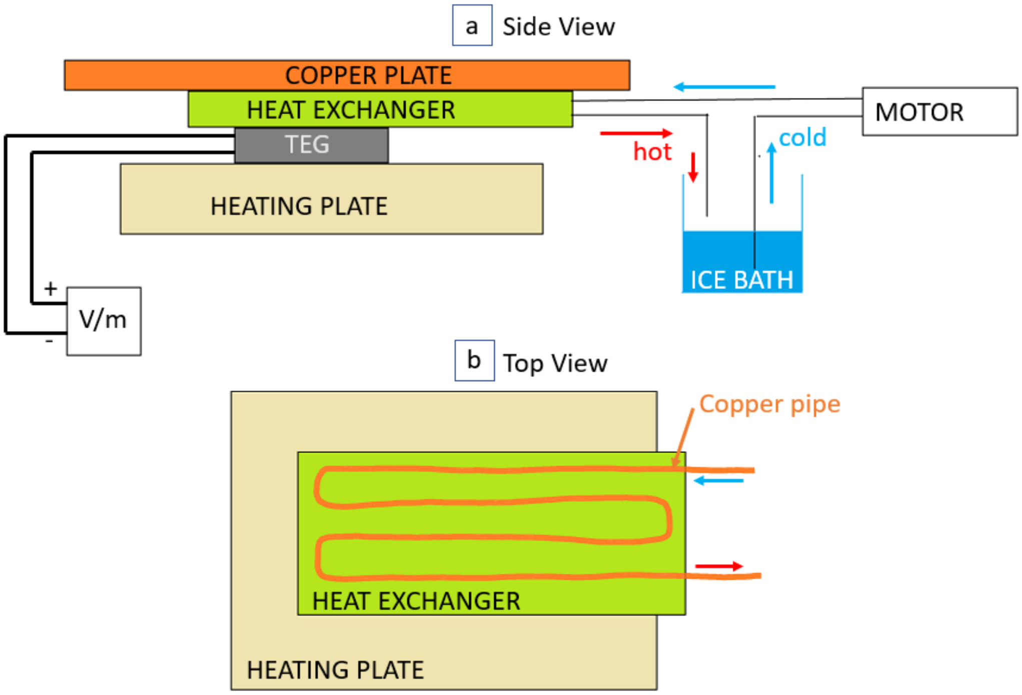

Figure 5: (a) Shows the side view of the setup for TEG testing. (b) Shows the top view with heat exchanger on top of heating plate. The copper plate placed on top of the heat exchanger stabilized the shaky heat exchanger caused due to the motor force. It also acted as a heat sink.

Test 3 replicated the setup of test 2, but with an ice bath circulating through the heat exchanger instead of the room temperature water. The ice bath was maintained at 0°C, with more ice added as needed. When the heating plate was set at 500°C, the voltage output was measured to be 1.45V.

According to the TEG specification [M1], the expected output for an open circuit with hot side temperature of 440°C and cold side temperature of 25°C is 4.5V. However, our experiment yielded the maximum voltage of only 1.45V. One possible reason for this discrepancy is the lower temperature on the hot side of the TEG. Despite setting the heating plate to 500°C, it is likely that the temperature on the hot side of the TEG was lower. This could be attributed due to the imperfect contact between the heating plate and the TEG surface.

In test 1, we measured higher voltage when an aluminum (Al) plate was placed on top of the TEG compared to using a lighter copper rod. It is plausible that the heavier Al plate exerted more pressure on the TEG, ensuring better contact with the heating plate. A similar increase in voltage was observed in Test 2 with the ring stand.

Additionally, the heating plate exhibited uneven temperature distribution, with the center being hotter than the edges. Although in test 2, the TEG was placed towards the edge of the plate for easier setup, we recognized the temperature gradient and repositioned the TEG at the center in Test 3 to maximize the temperature on the hot side. Silicon compound thermal paste was used to improve the contact between the surfaces; however, the paste quickly dried and began burning.

Water leaking from the pipe joints and motor was another issue encountered during the experiment. Despite using hose clamps, significant water was lost from these sights, requiring frequent refilling of the ice bath reservoir. A J-type thermocouple was used to monitor the ice bath temperature, which remained below 5°C throughout the experiment. The experiment was concluded due to excessive leaking from the motor.

2.1.2 Stainless Steel Testing

This testing aimed to assess the compatibility and durability of stainless steel when exposed to molten Al-Si. Existing studies show high reactivity between Al-Si and stainless-steel when in prolonged contact resulting in the dissolution of stainless steel [19]. To mitigate this issue various coatings such as boron nitride (BN) based coating [20] and MgO-Zr_2O_3 plasma-spray coating [19] have been investigated to prevent corrosion. In addition, numerous studies have explored alternative housing materials for Al-Si alloy [22], [23]. Despite the documented reactivity of Al-Si with stainless-steel, the specific grade of stainless-steel used was not specified. It was imperative for our bench-top demonstration that we verify the ability of our housing material to withstand the exposure to Al-Si at 600°C without leaking.

A 12 oz. 304 stainless steel cup with 400g of Al-Si was melted using a muffled furnace. In the first twenty-five hours at 600°C, no leakage was observed; however, leaking was observed after seventy hours. The prolonged contact between Al-Si and 304 stainless-steel dissolved the sides of the cup causing Al-Si to leak (Figure 7). While the bottom of the cup remained intact, there was Al-Si residue on the bottom that did not dissolve even after immersing the stainless-steel cup in Sodium hydroxide (NaOH) of 10 normality (N) solution for twenty-four hours. A similar test was conducted with 43.6 grams of Al-Si, yielding comparable observations. However, no leaking was detected even after forty-four hours at 600°C. This is possible due to the smaller quantity of Al-Si sample which resulted in less contact with the sides of the cup. As we noticed earlier the bottom of the cup demonstrated less susceptibility to leaking in comparison to the sides of the cup.

In addition, an identical experiment was conducted using alumina crucible. Consistent with the existing papers, alumina cups were found to withstand the Al-Si at high temperature and showed no interaction. The molten Al-Si demonstrated hydrophobic nature on the alumina surface, easily sliding through the crucible without leaving any trace.

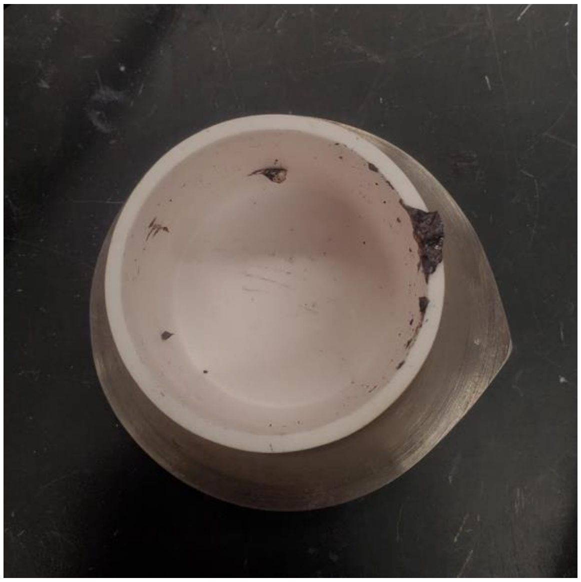

Figure 6: Demonstrates the alumina crucible after sixty hours exposure to molten Al-Si at 600°C. Unlike stainless-steel, the alumina crucible was gradually cooled down leaving it inside the furnace to prevent breaking due to thermal shock.

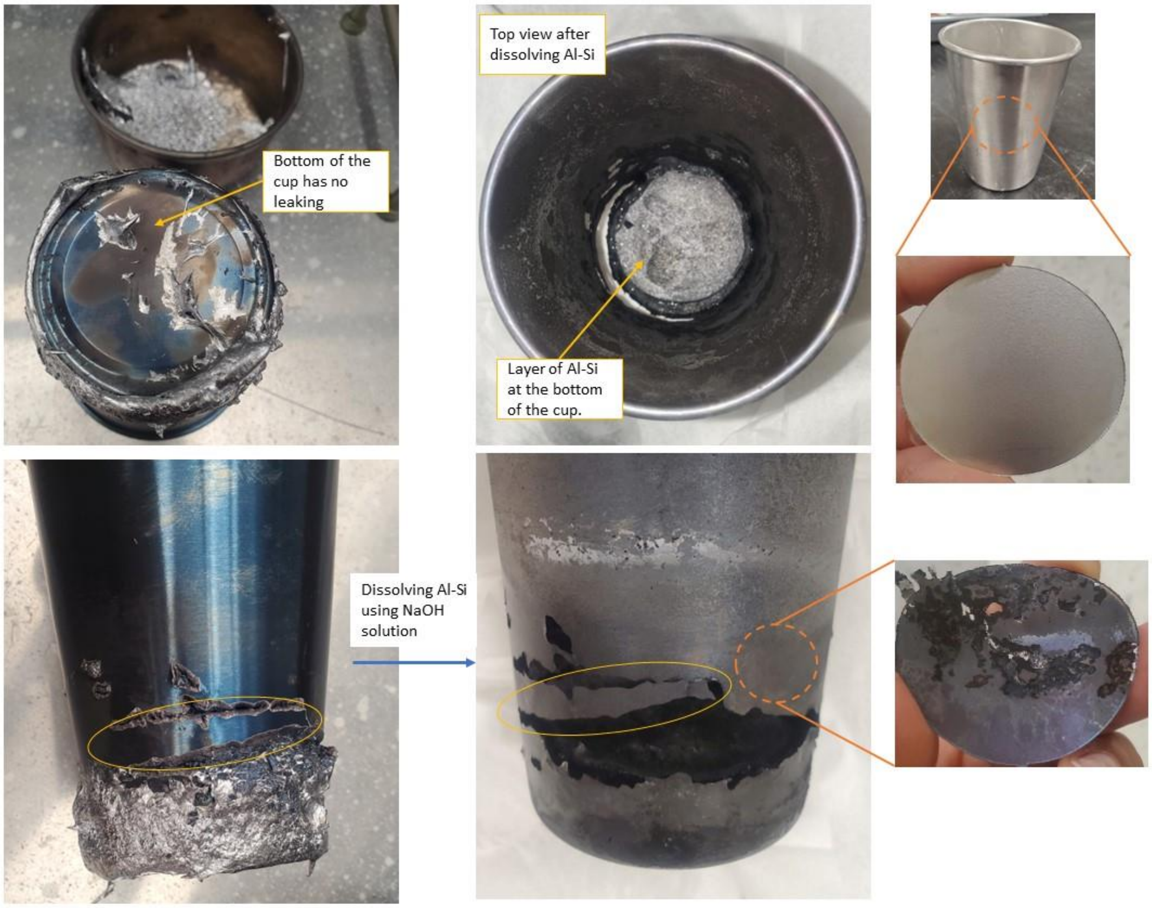

Figure 7: The image shows the condition of 12 oz. 304 stainless steel cup after approximately seventy hours at 600°C. While the sides of the cup were highly reactive to Al-Si, the bottom of the cup was intact. The presence of Al-Si at the bottom of the cup even after dissolution process prevented us from viewing the effect of Al-Si on the bottom surface using SEM. A small cutout from the side of the cup was taken for the SEM analysis.

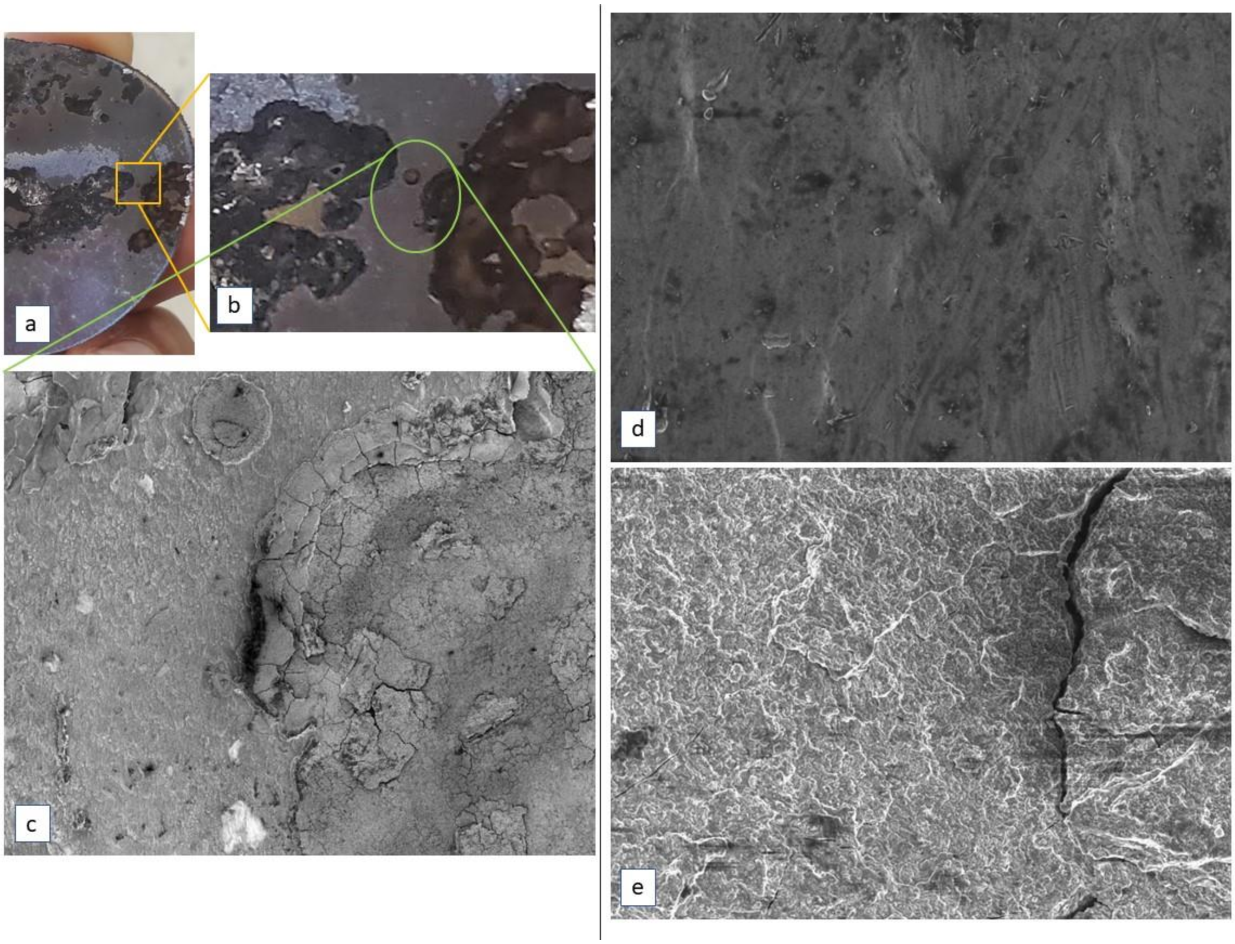

Figure 8: Shows the SEM image taken of the sample.

Scanning Electron Microscopy (SEM) was performed on the cutouts from Figure 7 to compare the morphological changes on the surface of the cup before and after exposure to molten Al-Si. Due to the limited field of view in SEM, capturing images at the edge presented difficulties. However, by utilizing the maximum zoom-out capability, SEM scanning of the section highlighted in Figure 8b was successfully achieved showing in Figure 8c. By examining the images taken at the boundary between corroded and uncorroded regions, we can directly compare the effects of Al-Si. Figures 8c and 8e reveal the effects of Al-Si, showing visible cracks. The darker areas within these cracks indicate deeper penetration. The images also show that the corrosion rate is not uniform throughout the stainless steel. Morphological changes are evident when comparing Figures 8c and 8e with the reference image 8d, which represents a scan of an unused stainless-steel cup.

2.1.3 Heater Testing

The purpose of the heater in this set up was to melt the Al-Si pellets. If Al-Si were to be used as the thermal storage material in the CSP technology the input energy would be the concentrated radiative energy from the sun, therefore the initial set up was chosen stimulate radiative heating like that of the sun. (Rea et al., 2018;2019) placed the resistive heater half an inch below the thermal storage tank to simulate radiative heat input from the sun [18][19]. In this testing we placed the heater at the center of the thermal storage tank as the prototype proposed by (Dering et al., 2019).

Table 2: Transformers and heater specification.

	Transformer 1	Transformer 2	Grainger Heater	Tempco Heater
Power [W]	2000	3000	2000	1000
volt [V]	220	220	240	240
current [A]	9.0909	13.6363	8.3333	4.1666
Resistance [Ω]	-	-	28.8	57.6

Table 3: Tempco Heter Specification when connected in parallel and series.

Heaters in	series	parallel
R [Ω]	115.2	28.8
V [V]	220	220
I [A]	1.909722	7.63889
P [Watt]	420.138	1680.55

Table 2 presents the current limitations and resistances for each transformer and heater, while Table 3 displays the resistance (R), voltage (V), current (I), and power (P) for Tempco heaters when connected in series and parallel.

2.1.3.1 Heater Testing #1

A ceramic tube (OD 1.875" x ID 1.625" x 8.500" Long) was placed in the center of a 1.25-liter stainless steel container. The half of the container was filled with Al-Si pellets. Inside the ceramic tube, a 2000W heating element from Grainger's was installed. Power for the heater was supplied by a 3000W transformer. This setup aims to replicate radiative heating conditions akin to sunlight [19]. The ceramic tube served to encase the heater, protecting it from potential corrosion caused by Al-Si. This choice was based on the high melting point of ceramics and their demonstrated resistance to interaction with molten Al-Si in previous experiments.

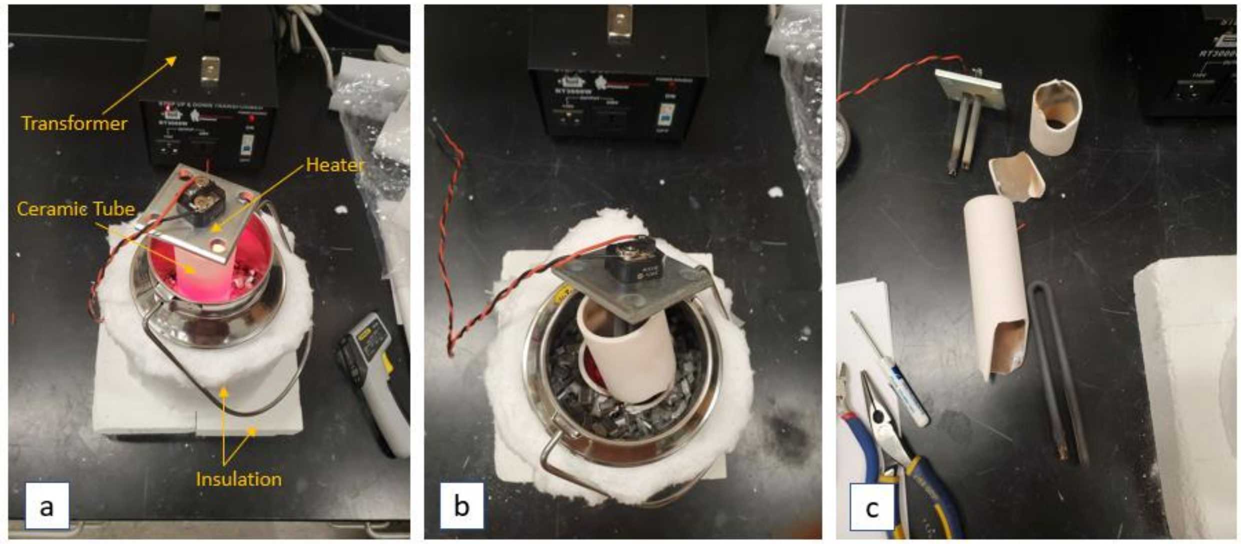

Figure 9: Shows the experimental setup of heater testing 1.

Within fifteen minutes of initiating the heating process, both the heater and the ceramic tube broke, and the fuse of the transformer was blown. Initially, the manufacturer's recommendation of a transformer power rating approximately 50% higher than the load power rating seemed to pose no issues. However, upon reaching a steady state, the resistance of the heater decreased due to the high temperature, while the input current and voltage remained constant. This resulted in the current exceeding the heater's limit for the corresponding resistance at that temperature, causing the heater to overheat and damage the circuitry. Additionally, the lack of proper heat dissipation was another contributing factor to the heater's failure. Since the heater was in contact with air, which has low thermal conductivity, there was minimal heat dissipation during overheating. Further investigation revealed that the heater was primarily designed for immersible heating applications. Collectively, all these factors contributed to the failure of the heater.

2.1.3.2 Heater Testing #2

Here, we used two Tempco Cartridge Heater [M4] placed inside the ceramic tube filled with aluminum oxide (Al_2O_3), with a power rating of 1000W and an operating voltage of 240V. The Tempco heaters are designed to withstand high temperatures up to a maximum of 1800°C and are applicable for radiative heating unlike Grainger’s heater. To power the heaters, a 2000W transformer was employed. In addition, to ensure safety, the stainless-steel container was insulated with thermal insulation blankets on the sides and placed atop thermal insulation sheets.

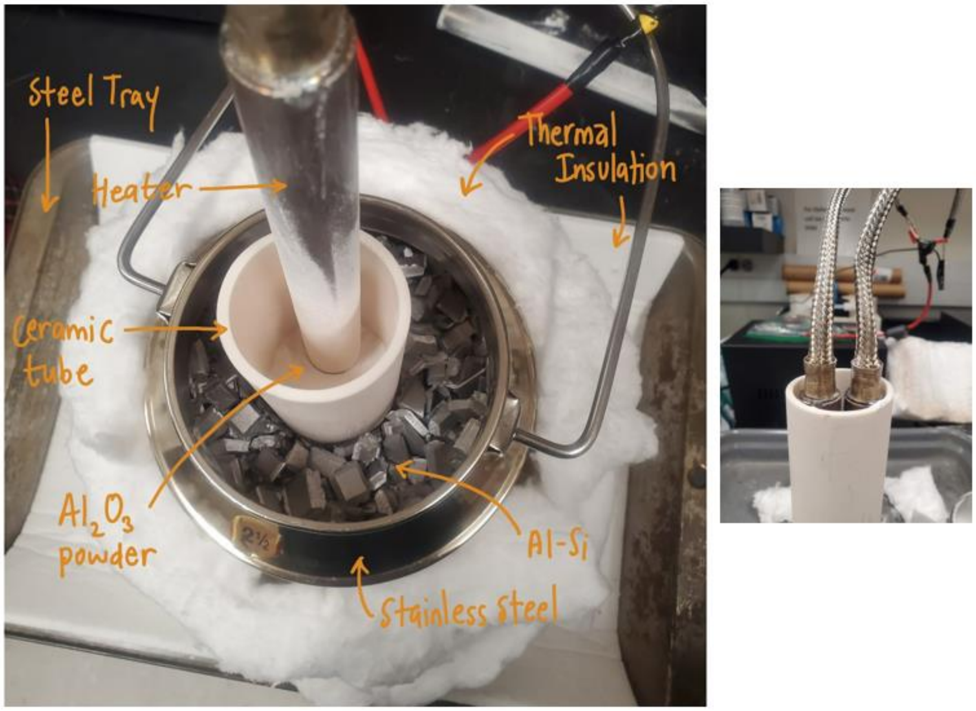

Figure 10: Shows the experimental setup of heater test 2.

In this test, no issues were encountered with the heaters. They were connected in series to reduce the current through the circuit and provide a sufficient margin to accommodate any fluctuations. Additionally, a 3-Amp fuse was included in the circuit for further protection. Although the use of series connection led to a longer heating time, it was necessary to prevent overheating and potential damage. While the current level for a parallel configuration of the heater would still fall within the current limit of the transformer (9.1 Amps), we opted for the safer option.

Furthermore, to address the heat transfer issues observed in the previous test aluminum oxide (Al_2O_3) powder [M7] was added inside the ceramic tube. This addition aimed to minimize the thermal discontinuities and improve heat dissipation. Although Al_2O_3 has significantly higher thermal conductivity than air and effectively minimizes thermal discontinuities inside the ceramic tube, the presence of imperfect contact between the Al-Si pellets and the ceramic tube, as well as between the Al-Si pellets themselves, resulted in the formation of air gaps. These gaps contributed to thermal inconsistencies within the system. On the other hand, adding Al_2O_3 also deviated from simulating the sun-like radiative heating.

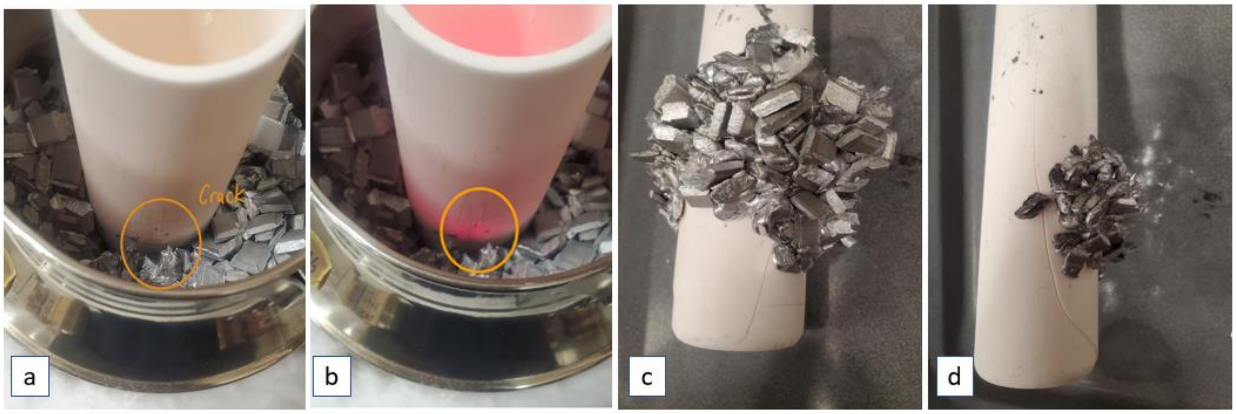

Figure 11: Shows the crack on the ceramic tube.

During the experiment, the heater was operated for approximately 3 hours on the first day and 5 hours on the second day before being turned off upon noticing a crack in the ceramic tube as shown in Figure 11. The crack, particularly visible in Figure 11b under red light illumination, extended down to the bottom of the ceramic tube. The adhesion of Al-Si on one side of the ceramic tube indicated localized temperature reaching 577°C, suggesting non-uniform heat transfer.

Ceramic tubes, being brittle with low tensile strength, are susceptible to sudden temperature change and non-uniform temperature gradient, making them prone to cracking and breaking. Additionally, only a portion of the outer surface of the ceramic tube was in direct contact with the Al-Si, leaving the rest exposed to air. This led to non-uniform heat transfer through the ceramic tube. The resulting thermal gradient within the tube likely caused uneven expansion, leading to the generation of stress, and ultimately resulting in the crack observed in the ceramic tube.

2.2 Experiment Summary

The bench-top system aimed to showcase small-scale thermal energy storage using eutectic Al-Si alloy. Subsystem feasibility was assessed through experiments. Results from thermoelectric generator testing revealed that while TEGs can convert thermal energy to electrical energy, practical output requires a larger quantity. TEG's lower efficiency and imperfect contact with surfaces on both hot and cold sides lowered its overall output. Additionally, 304 stainless-steel proved unsuitable for long-term containment of molten Al-Si due to corrosion issues. Likewise, the heating setup implemented in this experiment was inefficient due to thermal inconsistencies and non-uniform heating. While the demonstration of benchtop LHB wasn't entirely successful, it serves as a valuable stepping-stone for advancing research in the field of latent heat batteries. It also proves that extensive preliminary research is needed before starting this grand and interdisciplinary project.

CHAPTER 3: MATHEMATICAL ANALYSIS

3.1 Introduction

The purpose of this analysis is to perform the first-order sensitivity analysis on the thermal storage container parameters such that Al-Si is maintained at 577°C for 32 hours. This mathematical analysis is conducted in section three (S3) of the diagram in figure 12. In this section, Al-Si is molten at 850.15 K.

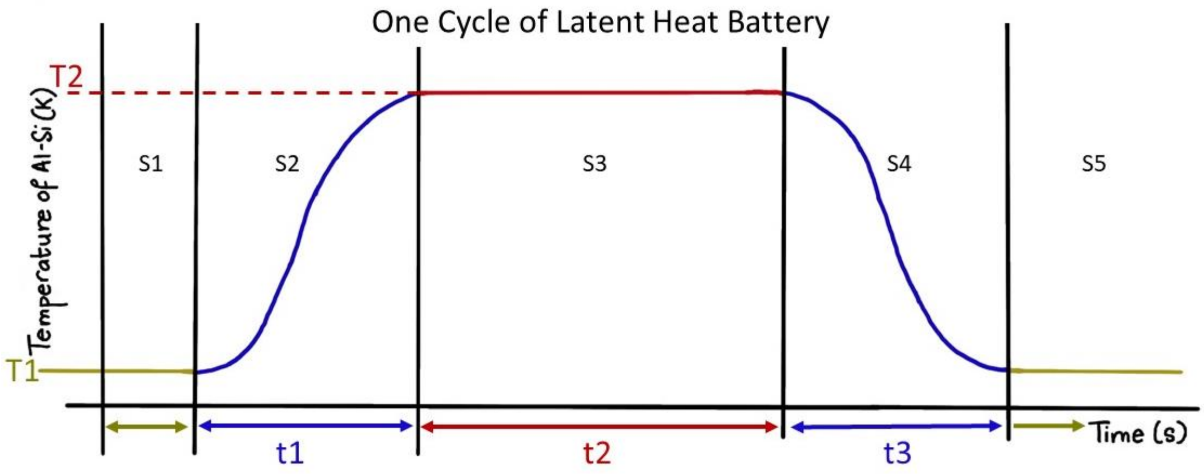

Figure 12: Shows the one cycle of the latent heat battery.

3.1.1 Assumptions

The following assumptions are made in this study:

1. Isothermal process. Throughout this sensitivity analysis the temperature of Al-Si is fixed at 577°C (850.15 K).
2. One dimensional heat transfer. Only heat loss in radial direction is considered. The heat loss from surface 2 and surface 3 in Figure 13 is ignored.
3. Sensitivity analysis is conducted after numerous cycles presented in Figure 12. This allowed us to exclude the time taken to melt the given mass of Al-Si for the very first time. Therefore, we assume that for any subsequent cycle, the Al-Si will only take 10

hours to reach PCT, regardless of the mass (time_of_phase_change = 10 hrs.). In addition, the method of melting Al-Si is not critical.

4. Material properties are uniform. Thermal conductivity and emissivity do not depend on temperature.
5. Thermal reflection, absorption, and transmission are ignored. Only radiative emission is considered.
6. The surface of the container is gray (emissivity (ε) = absorptivity (α)), diffuse, and opaque.
7. Radiative loss between the surface of molten Al-Si and the top of the container is not considered in the analysis.
8. Perfect contact between the layers, meaning there are no air gaps.
9. Ignored boundary conditions. While a detailed conduction analysis could be conducted at the boundary between the molten Al-Si and alumina surface, we assume the temperature to be initially 850.15 K.
10. Thermal storage tank is not exposed to moving air, therefore convective loss is negligible.
11. For simplification of calculation,

    r_inner = ½ height of container.
12. Temperature distribution is uniform over the surfaces and molten Al-Si.
13. Thickness of material layers will not affect the emissivity value of respective layer material.
14. In figure 13, the only surface seen by the radiation leaving the inner surface is the outer surface. F_{ij} (view factor) is defined as the fraction of the radiation leaving surface i that

strikes surface j directly. Since the entire radiation emitted from the inner surface is intercepted by the outer surface, the view factor is 1.

$$F_{Ag\rightarrow SS} = 1$$

3.1.2 System setup

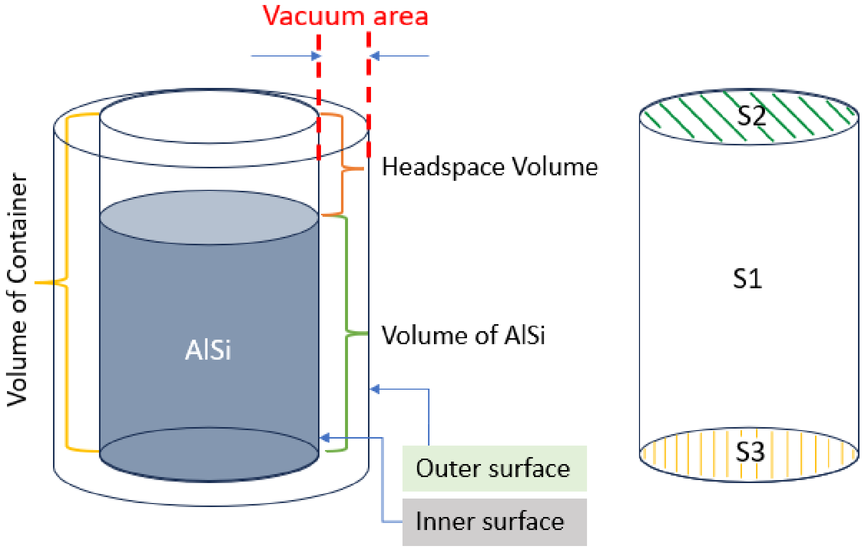

Figure 13: Shows the cylindrical container selected for this analysis. S1: Surface 1, S2: Surface 2, S3: Surface 3. The gap between the top of the container and the surface of the Al-Si alloy is called the headspace. It is expressed as a percentage value in this analysis. Here, the inner surface and outer surface are at r_3 and r_6 in Figure 15 respectively.

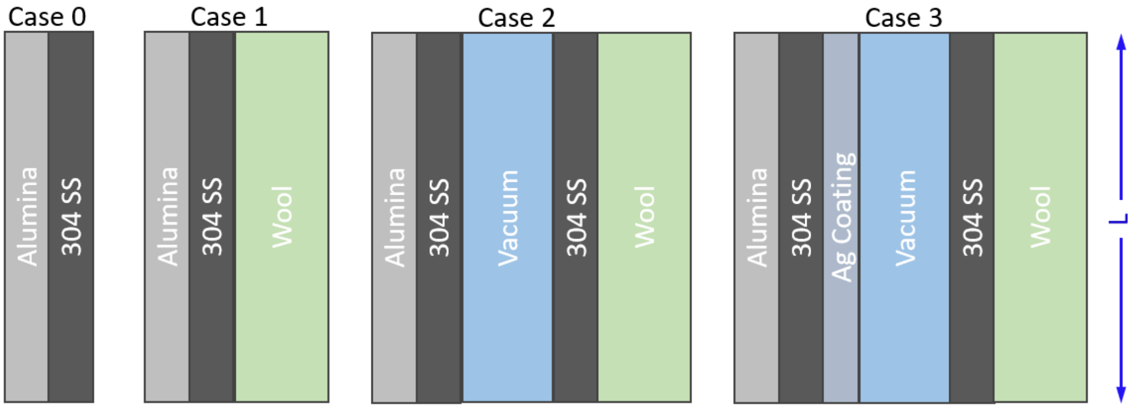

Figure 14: The configurations shown above represents the layers of the thermal storage container. The respective layers are informed by research and analysis from benchtop prototype.

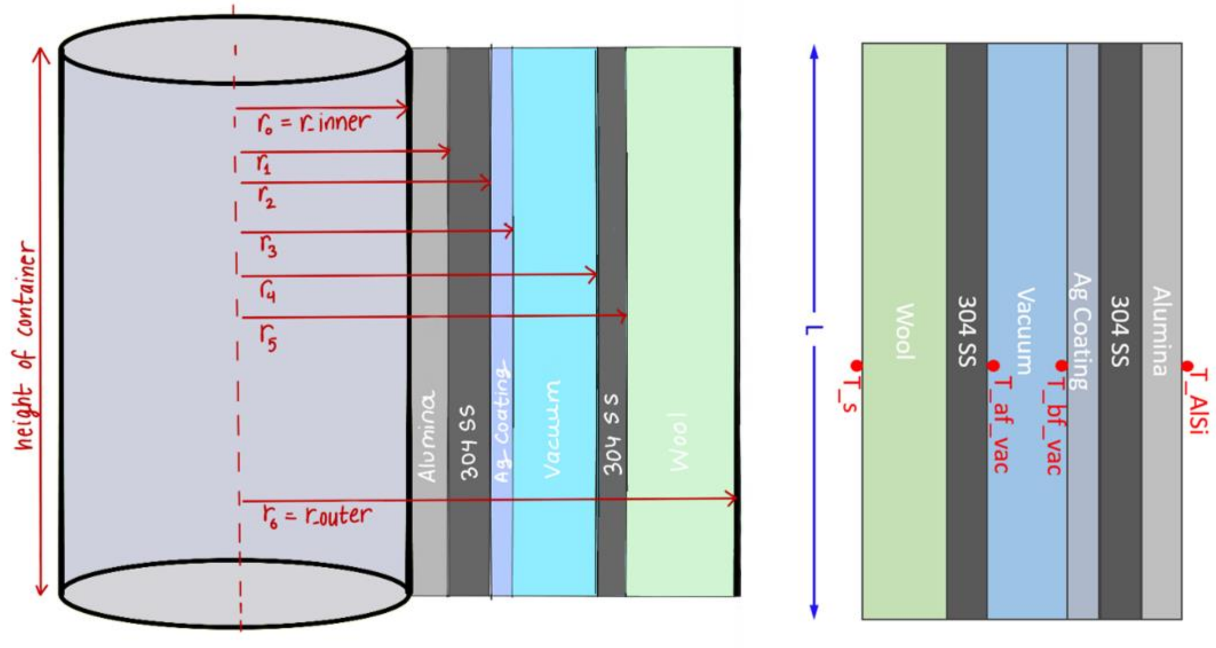

Figure 15: Shows the storage container design with radius and temperature labeled.

3.2 Method and Procedure

This section discusses the process taken for performing sensitivity analysis. Sensitive analysis determines how different values of an independent variable affect a particular dependent variable under a given set of assumptions [43]. The independent variables in this analysis are the input variables. We will analyze how the dependent/target variables are affected by changes in input variables. This will be quantified based on percent change.

The **input variables** are as follows:

1. Emissivity
    a. Silver (epi_ag)
    b. Wool (epi_wool)
2. Headspace (headspace)
3. Thickness of layers
4. Temperature (shown in figure 15)

   a. Outer surface (T_s)
   b. Surface in-contact with Al-Si (T_alsi)
   c. Surface before vacuum (T_bf_vac)
   d. Surface after vacuum (T_af_vac)

The **target variables** are as follows:

1. Radiative loss
   a. The radiative loss for the outermost layer is given by [48]:

$$Q_{rad} = A * \sigma * \varepsilon * \left(T_{surface}^4 - T_{surrounding}^4\right)$$

where:

A = Area of the surface radiating $[m^2]$

σ = Stefan-Boltzmann constant $\left[\frac{W}{m^2K^4}\right]$

ε = Emissivity of radiating surface

$T_{surface}$ = Temperature of the surface radiating heat. [K]

$T_{surrounding}$ = Temperature of the surrounding [K]

   b. The radiative loss for the vacuum layer is given by [49][50]:

$$\frac{A_1}{A_2} = \frac{r_1}{r_2};\ F_{12} = 1; Q_{12} = \frac{A_1\sigma(T_1^4 - T_2^4)}{\frac{1}{\epsilon_1} + \frac{(1-\epsilon_2)}{\epsilon_2}\left(\frac{r_1}{r_2}\right)}$$

where:

F_{12} = View factor from inner surface to outer surface (Figure 13)

ε_2 = Emissivity of the surface right after vacuum

ε_1 = Emissivity of the surface right before vacuum

2. Conductive loss

Calculated using 1D-cylindrical thermal resistance model where if we have a composite structure with multiple layers than conductive loss is the ratio of the temperature difference (ΔT) across the material to the sum of thermal resistance ($R_{rad,total}$) of the layers in radial direction.

$$Q_{cond} = \frac{(\Delta T)\ [K]}{R_{rad,total}\ [\frac{K}{W}]};\ \ R_{rad,total}\ = \sum_{n=0}^{N} \frac{ln\left(\frac{r_{n+1}}{r_n}\right)}{2\pi k_{n+1} L}$$

where:

N: Number of layers (In case of figure 15, we have six layers. n = 0 will be the $r_0 = r_{inner}$ and $r_N = r_6$)

k = Thermal conductivity of that layer. $\left[\frac{W}{m*K}\right]$

L = Height of the container. [m]

3. Surface area to volume ratio

We want a lower surface area to volume ratio. The object with higher surface area to volume ratio tend to lose heat more rapidly. Larger surface area allows for more efficient heat transfer between the object and its surrounding.

$$SAV = \frac{(surface\ area\ of\ the\ outer\ layer)}{volume\ of\ Al-Si}$$

4. Time

We want to increase time. In Figure 11, labeled as t2.

$$time = \frac{total\ latent\ heat\ energy\ [J]}{Q_{loss}\ [W]}$$

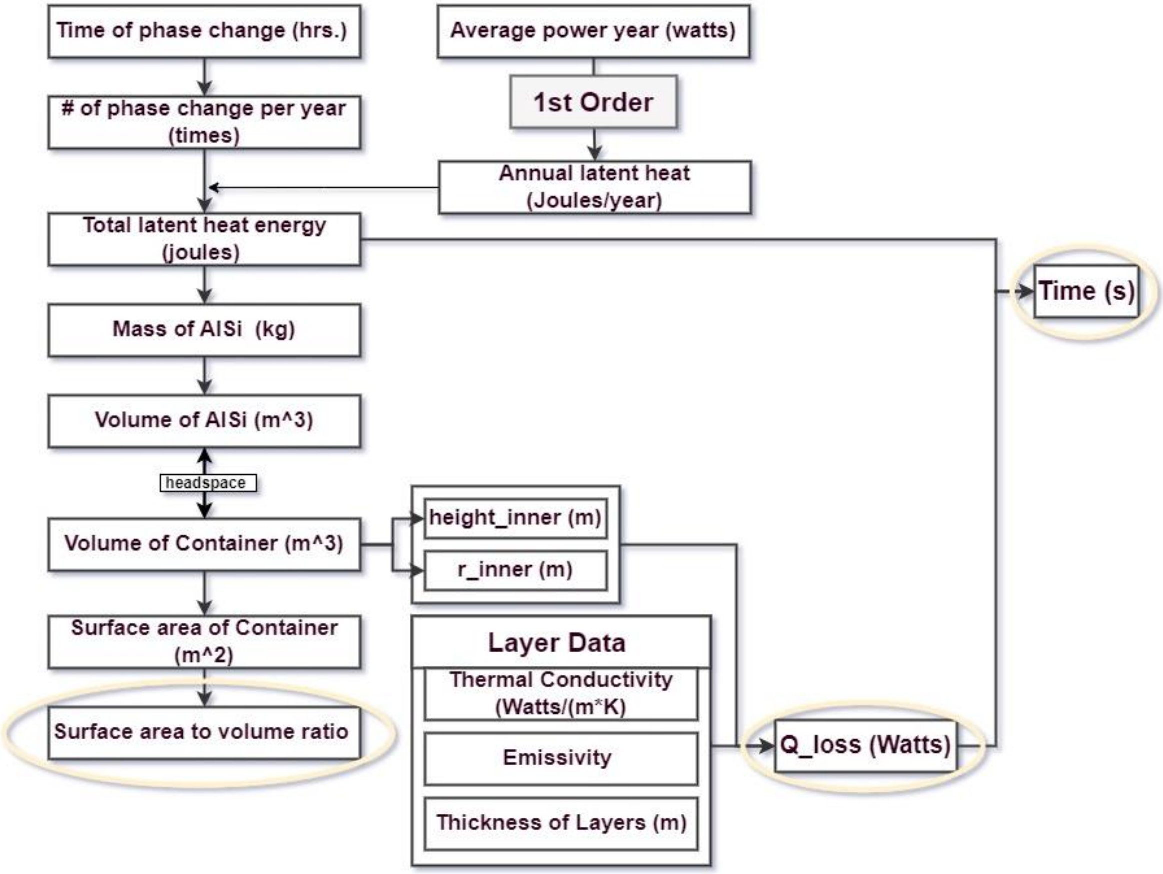

Figure 16: The above flow charts show the steps taken to calculate the target variables.

In 2021, the average annual amount of electricity sold to a U.S residential electric-utility customer was 10,632 (kWh), with Louisiana having the highest annual electricity purchases per residential customer at 14,302 kWh and Hawaii having the lowest at 6,369 kWh per residential customer [45].

The calculation begins with annual electricity consumption of a U.S. household, which is converted into power, denoted as average power per year [W]. Using this power value, latent heat energy [Joules/Year] and total latent heat energy [Joules] are calculated. Latent heat of fusion [Joule/kg] is used to determine the mass [kg] required to produce this energy, and the density of Al-Si is used to compute the volume of the material. Using volume of Al-Si and the headspace value discussed in Figure 13 is used to obtain the volume of the container.

Additionally, assuming that the inner radius (r_{inner}) equals half the inner height, we calculate r_{inner}. The value along with the given thickness, allows calculation of the container's surface area at the respective radius. By considering the surface area of the outer layer and the volume of the Al-Si, we determine the surface area-to-volume ratio. Similarly, layer data, a data structure containing the layer's name, thickness, and thermal conductivity, and emissivity is used to calculate the heat loss (Q_{loss}). Q_loss [W], along with previously calculated latent heat energy, is then used to determine the time during which the Al-Si will remain at 577°C.

3.3 Results

3.3.1 Phase 1

In phase 1, we examined different cases (0,1,2, and 3 shown in Figure 14) by varying the headspace percentage (0,1, 5, 10, and 20 percent). The values utilized in Phase 1 calculation are detailed in Appendix I. Initially, the temperatures at various layers and the thickness of layers are estimated through educated guesses. We will consider the upper limit of the annual electricity consumption of a household for further analysis since this will yield maximum mass which satisfies the energy requirement for both minimum and average annual electricity consumption.

For the phase change time of ten hours and maximum annual electricity demand of "a" U.S. residential utility customer being 14 kWh/year, the average power per year is 1632 kW. This yields the annual latent heat of $5.149 \ast 10^{10}$ Joules/year and total latent heat of 58775342.47 Joules for eight hundred seventy-six phase changes per year. To yield the calculated total latent heat, we require 125.0539 kg of Al-Si. Adding kaowool insulation in Case 1 reduces conductive loss by 99.92% compared to Case 0, where only alumina and stainless-steel are present. Although Case 0 is not practical, it serves as a baseline to observe the impact of kaowool insulation on conductive loss. In cases 2 and 3, which involve vacuum layer, conductive loss is calculated both before and after the vacuum layer. It was noticed that the presence of silver coating does not make a huge difference given the thickness of the coating. However, the conductive loss before the vacuum is the main contributor to the total heat loss of the system, showing more than 87.7% for case 2 and 98.5% for Case 3. Radiative loss occurs at two locations: the outer layer and the vacuum layer. Radiative loss in the outer layer contributes less than 2% to the total heat loss for all cases and headspaces. However, in Cases 2 and 3, there is also radiative loss in the vacuum, which decreases by 95% in Case 3 compared to Case 2 due to addition of a silver coating. The emissivity of the silver coating is 0.03, whereas that of 304 stainless steel is 0.757, meaning stainless-steel surface emits a lot more thermal energy than silver. Despite this, the radiative loss in the vacuum itself contributes less than 12% to the total heat loss of the system, which is a lot less than the 88% contributed by conductive loss before vacuum.

Similarly, the longest time of 18.39 hours is calculated for Case 1 with headspace of zero percent. Even when the headspace is 20% the time only drops to 16.36 hours. The addition of kaowool in Case 1 significantly increases time compared to Case 0. The thermal conductivity of Kaowool is significantly lower than that of 304 stainless steels, which makes it a good insulator, decreasing conductivity loss and increasing the time. The longest time is calculated for Case 1, followed by Case 3, which still shows considerable reduction (98%) compared to Case 1 despite its more complex layer configuration.

For the specified structural parameters, the lowest surface area to volume ratio (SVR) was attained in Case 1 with 20% headspace. While SVR was initially regarded as one of the target parameters, subsequent adjustments were not focused on further reducing the SVR.

From phase 1 calculation, Case 1 and Case 3 emerge as the most promising candidates for further analysis, with Case 1 being particularly effective. Conductive heat loss is found to be a primary contributor to overall heat loss, especially in configurations involving a vacuum conductive heat loss before the vacuum plays a substantial role. Moving forward, our aim is to reduce heat loss adequately to achieve the target time of 32 hours within the physical constraints and assumptions.

3.3.2 Phase 2

3.3.2.1 Part 1

In part 1 of phase 2, we explore the effects of percentage variation in input variables on the target variables. The mass of the Al-Si is 125.054 kg. Similarly, in phase 1, we varied cases and headspace percentages. In Phase 1, we explored various cases and headspace percentages, narrowing out focus to Case 1 and Case 3 for further analysis in Phase 2. Additionally, based on practical considerations outlined in [47], a 5% headspace is deemed practical. Our objective is to understand how changes in input variables impact the target variables, allowing us to optimize parameters to meet desired target variable. We aim to address questions such as: What percentage of change in an input variable causes a corresponding change in a target variable? Which input variable exhibits the highest sensitivity with the system. Given the multitude of input variables, our analysis focuses on assessing the impact of varying each input variable individually on a target variable. Certain input variables exclusively influence Case 3, while others affect both Case 1 and Case 3. Our objective is to decrease the emissivity of the materials to mitigate radiative loss. Although the emissivity value utilized in phase 1 is based on research, we explore the impact of further reducing emissivity on the target variables. This analysis will enhance our understanding of the crucial role emissivity plays in achieving the desired target variables.

Additionally, we examine the effects of altering layer thickness and temperatures at different boundaries on the target variables. The calculation methodology mirrors that of Phase 1, but now we generate a list of input variables indicating percentage changes from the original values. Positive values in the percentage change list represent a percentage increase in the original value, while negative values represent a percentage decrease.

For Case 1, according to Table 27, decreasing emissivity by 0.5% yields only 0.0077% percent increase in time. Among different temperatures (T_alsi, T_surr, and T_s), notably changes in T_alsi have the most significant impact on time, with a 2% decrease resulting in a 3.1385% increase. Conversely, a 2% increase in T_surr and T_s decreases radiative loss at from outer layer by 83.2289% and 86.1454% respectively, but this translates to only minor increases in time of 1.2973% and 0.2524% respectively. This shows that the contribution of radiative loss from the outer layer to total loss is negligible. Similarly, reducing the thickness of alumina and stainless steel 1 by 20% results in a time increase of 0.2309% and 0.2262%, respectively. Conversely, a 20% increase in the thickness of wool leads to a time increase of 18.2565%.

For Case 3, according to Table 28, a 0.5% decrease in the emissivity of kaowool and silver only results in a time increase of 0.0001% and 0.0031%, respectively. Additionally, a 0.5% increase in temperature before vacuum decreases conduction before vacuum by 16.4015% and increases time by 19.2685%. The impact on T_s and T_surr mirrors that of Case 1, albeit achieved with a 2% decrease in T_s and a 2% increase in T_surr for Case 3. Likewise, reducing T_alsi by 2% led to a significant decrease of 67.6063% in conduction before vacuum and a considerable increase of 199.89% in time. A 2% decrease in temperature after vacuum reduces conductive loss after vacuum by 4.66% and extends time by 0.0255%. Increasing the thickness of alumina by 20% reduces conductive loss before vacuum by 6.4% and extends time by

6.7308%. Likewise, increasing the thickness of stainless steel 1 reduces conductivity loss before vacuum by 11.3477% and increase time by 12.5932%. Conversely, a 20% reduction in the thickness of both the vacuum and stainless steel 2 marginally increases time by 0.00864728% and 0.001652196%, respectively. Notably, altering the thickness of wool has minimal impact on time, with only a 0.118199823% increase despite a 15.77868% decrease in conductive loss after vacuum.

From our analysis, it becomes evident that emissivity has minimal impact on the total loss of the system, as radiative loss isn't the primary contributor. Instead, conductive loss, particularly before vacuum, emerges as the most significant factor influencing overall loss. Decreasing conductive loss, especially pre-vacuum (in Case 3), notably extends the operational time. For Case 1, T_alsi appears to exert the most significant influence on increasing time. While T_surr and T_s does affect radiative loss, it doesn't notably impact the time due to radiative loss not being the primary contributor to total loss. In contrast, for Case 3, T_alsi and T_bf_vac exhibit the most substantial effect, decreasing conductive loss before vacuum and consequently extending the operational time significantly. T_s and T_surr affect radiative loss from the outer layer similarly to Case 1. T_af_vac decreases conductive loss after vacuum, resulting in a notable increase in time. Increasing the thickness of layers before vacuum reduces conductive loss before vacuum, consequently increasing the operational time. Likewise, increasing the thickness of kaowool decreases conductive loss after vacuum. Although decreasing the thickness of vacuum and stainless steel 2 does lead to a time increase, it's by less than 0.01%. Conductive loss before vacuum is the primary cause of loss in the system. For both cases, setting T_alsi to 833.147 K results in the longest operational time (18.3882 hrs. for Case 1 and 0.9311 hrs. for Case 3) compared to other input variables. In practical scenarios, T_alsi can vary, with higher values leading to shorter operational times and lower values resulting in longer times. Surprisingly, T_alsi equal to 850.15 K yields a shorter time than 833.147 K. More on T_alsi is analyzed in Phase 2, part 2. Consequently, increasing the wool thickness by 20% resulted in a time of 21.08362 hours, with T_alsi set at 850.15 K and all other parameters unchanged from phase 1. This reaffirms the superiority of Case 1 as a storage configuration for a latent heat battery.

3.3.2.2 Part 2

In part 2, we delve into methods for adjusting the input variables to attain the desired time. For both cases, the target time is established as 32 hours. To elucidate, this denotes the duration for which the Al-Si sustains the phase change temperature even after the heat supply is discontinued. This interval is defined as 'time' in our calculation.

3.3.2.2.1 Case 1

Constraints:
T_s = 300 K
T_surr = 298 K
epi_wool = 0.6, epi_ag = 0.03

To address safety concerns, we have imposed a constraint on the surface temperature T_s, setting it to 300 K (27°C) to ensure it remains above hazardous levels. Similarly, the surrounding temperature T_surr is fixed at 298 K (25°C). We begin by setting T_alsi to 850.15 K, and then adjust the thickness of the wool layer thik_wool_m to observe the resulting changes in time (presented in Table 11). All other parameters remain consistent with those of phase 1, except for the T_alsi value.

Table 4: Shows time for different thickness of kaowool for 0.1 in" thickness of the first stainless-steel layer.

thik_ss1_m = 0.1 in”	
Thickness of wool (in”)	Time (hrs.)
1	18.02482325633069
1.2	21.36462256677735

In the prototype latent heat storage system utilizing Al-Si as a phase change material and incorporating a Stirling engine for electricity generation [18], a stainless-steel casing of 1.5 mm (0.05 inches) thickness is employed for 100 kg of Al-Si. Similarly, in the advanced thermal storage system employing novel molten salt [44], a stainless-steel thickness of 0.75 inches is utilized for 400 kg of salt. To ensure a conservative approach, we will adopt the larger value for thik_ss1_m as it represents a more challenging scenario, set at 0.75 inches. Following the adjustment of the SS1 thickness, the updated values are shown in Table 12. It's noted that with an increase in the thickness of SS1, the time decreased.

Table 5: Shows time for different thickness of kaowool for 0.75 in" thickness of the first stainless-steel layer.

thik_ss1_m = 0.75 in”	
Thickness of wool (in”)	Time (hrs.)
1	16.7984542112628
1.2	19.91548615130966

In the advanced thermal storage system with novel salt [44], the thickness of the ceramic blanket is 10 inches. Now, we will begin increasing the thickness of the kaowool and see its impact on time and heat loss, shown in Table 13 below. It's important to note that we have not yet manipulated the thickness of the alumina.

Table 6: Shows calculated time and Q_loss for various thickness of kaowool.

Thickness of wool (in”)	Time (hrs.)	Q_loss (Watts)
1	16.79845	971.90395
1.2	19.91548	819.78837
2.05	32.41844	503.61706
2.5	38.59134	423.06076
3	45.12307	361.82116
6	78.36645	78.366456
10	111.1570	146.87767

When plotting data in Table 29, we observe the following trend show in the graph below. Analyzing the graph, we find that $Q_{loss} \leq 510.2026\, Watts$ will meet the target time of 32 hours. Since we achieved the target time without reducing T_alsi, we will maintain T_alsi at 850.15 K. Time and total loss (Q_loss) can be estimated from the thickness of wool using polynomial and power approximations respectively, as follows:

$$Time = -0.6328\, x^2 + 16.691x + 0.7801$$

$$Q_{loss} = 963.03 * \ x^{-0.879}$$

The average discrepancy for time is 0.14% and for total loss (Q_loss) it is 1.01%.

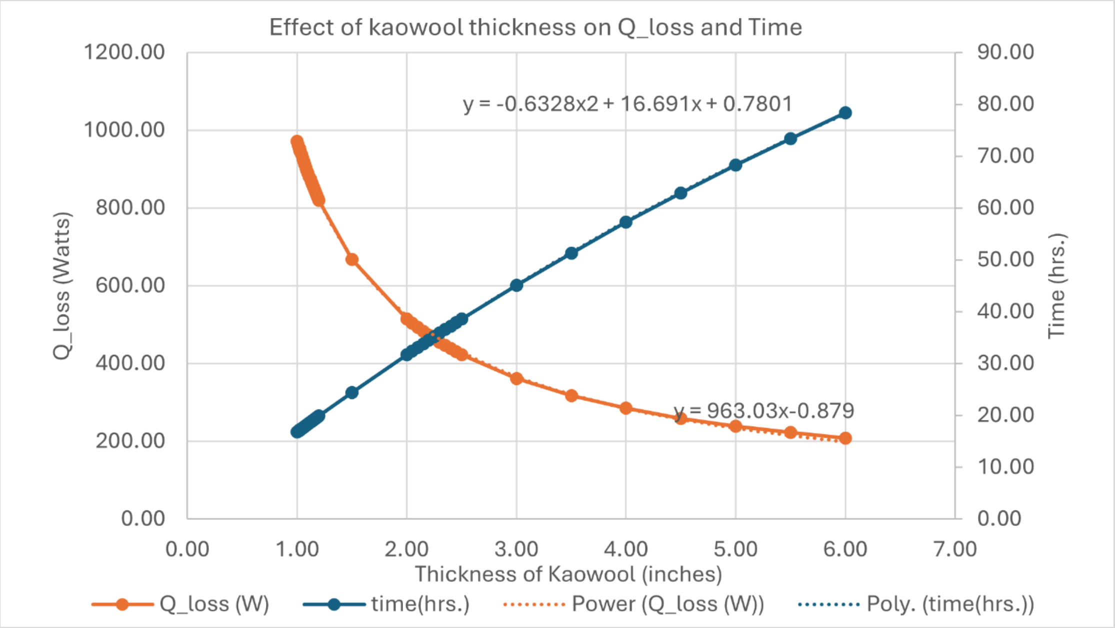

Graph 1: Shows the effect of kaowool thickness on Q_loss and Time.

Currently, the thickness of alumina is only 0.1 in”. An increase in thickness leads to a decrease in time. For a thickness of alumina equal to 0.75 in”, which is 86.66% higher than the previous value, we observe only a 6.66% decrease in time updated in Table 14.

Table 7: Shows the time and Q_loss for alumina with thickness of 0.75 in".

Thickness of wool (in”)	Time (hrs.)	Q_loss (Watts)
1	15.71225	1039.093
1.2	18.63441	876.1472

1.5	22.90325	712.8457
2.05	30.39364	537.1677
2.5	36.22124	450.7434
3	42.40297	385.0316
6	74.10239	220.3233

Despite adopting a more conservative approach, wherein T_s is set at 300K, T_surr at 298K, and T_alsi at 850.15K, and with the thickness of alumina and stainless steel at 0.75 inches, along with just 2.5 inches of thermal insulation provided by kaowool, we are able to achieve a time of 36.22 hours with a heat loss of 450.74W.

3.3.2.2.2 Case 3

Reducing thik_vac_m by 20% results in a negligible increase in time by only 0.00865%. Therefore, we will disregard this adjustment, maintaining the thickness of vacuum at 0.5 inches for the remainder of the calculation. Similarly, increasing the thickness of the silver coating by 20% only yields a negligible decrease in total loss by -0.04741% and an increase in time by 0.04743%, compared to the effects of other parameters. Hence, we will ignore this adjustment and set the thickness to be 0.01 inches. Other variables influencing Case 3 include the thickness of alumina, thickness of wool, thickness of the second stainless-steel layer, temperature before vacuum, and temperature after vacuum. Initially, epi_ag is set to 0.03; however, we will examine the consequences of its adjustment subsequently.

Constraints:
T_s = 300 K
T_surr = 298 K
epi_wool = 0.6, epi_ag = 0.03
Thickness of Ag coating = 0.01 in”
Thickness of vacuum = 0.5 in”
Thickness of first stainless steel layer = 0.75 in”

Starting with T_alsi = 850.15 K and thik_of_wool = 6 in”, while maintaining the values of all other parameters consistent with those of phase 1, we will now investigate the percentage change for the second stainless steel layer.

Table 8: Effect of change in thickness of the second stainless layer on time.

thickness of ss2 (in”)	time (hrs.)
0.1	1.51033974
0.75	1.5096

A 20% decrease in the thickness of the second stainless steel layer will increase time by only 0.001652%, a very small value compared to changes caused by other parameters. In Table 15, the thickness of second stainless-steel layer (SS2) is set equal to that of first stainless-steel (SS1) and the time decrease is 0.04857%. Therefore, the thickness of the second stainless steel is also constrained and set to 0.1 inches.

On average, 88% of the total loss is conductive loss before vacuum, and approximately 9.4% is from radiative loss in the vacuum. Now, we analyze the percent change for temperature after vacuum. T_alsi remains at 850.15 Kelvin, the thickness of wool is 6 inches, and the thickness of alumina is 0.1 inches. The temperature before vacuum is 825 K. In part 1 of phase 2, we observed an increase in time with a decrease in temperature after vacuum. However, here, we observe time increasing with an increase in temperature after vacuum. A 2% increase in temperature after vacuum increases time by 0.01574%, while a 20% increase in T_af_vac only increases time by 0.3197%. For now, we will leave T_af_vac at 525 K.

Now, we examine the percentage change for temperature before vacuum. From part 1, we know that an increase in T_bf_vac has a positive effect on time. T_bf_vac = 849.75 K yields a time of 24.411 hours with conductive loss before vacuum only 164.76 W. In this situation, 24.64% of Q_loss is contributed by conductive loss before vacuum and 61.30% by q_rad_vacuum. When T_alsi = 850.15 K, it is not reasonable for T_bf_vac to be 849.75 K. Therefore, we need to explore other ways to increase the time.

We now increase the thickness of the wool to 10 inches and again examined the percentage change for temperature before vacuum. Considering the advanced thermal storage system with novel molten salt utilized 10 inches of ceramic blanket for 400 kg of phase change material, maintaining a thickness of kaowool at 10 inches remains reasonable and practical. Increasing the thickness of kaowool to 10 inches resulted in a decrease of 31.78% in conduction after vacuum and a reduction of 10.99% in total conductive loss. Conversely, it led to an increase of 26.23% in outer layer radiative loss and a 4.02% increase in time. It had no effect on conductive loss before vacuum and radiative loss in the vacuum, as expected.

In our ongoing analysis, we now focus on adjusting the thickness of the alumina layer. Initially set at 0.1 inches, the alumina layer's thickness is up for reconsideration. With key parameters like T_alsi = 850.15 K, T_af_vac = 525 K, T_bf_vac = 849 K, and a wool thickness of 10 inches remaining constant, our aim is to enhance system performance. Previous observations suggest that increasing the alumina thickness yields positive results for operational time. For instance, increasing it to 0.75 inches, a substantial 650% increase from the initial value, results in a noteworthy 11.63% extension in operational time. This adjustment significantly reduces conductive loss before vacuum by 26.98%. However, it also leads to an increase in radiative losses. Despite these trade-offs, the optimal time achieved under these conditions is 18.58 hours. At this stage of the calculation, the contributions to Q_loss from various sources of loss are shown in Table 16.

Table 9: The contribution to Q_loss from different type of losses.

% Loss contribution to total Q_loss	
q_bf_vac	41.92948081
q_af_vac	7.093805783
q_cond	49.02328659
q_rad_vacuum	49.93656247
q_rad_outer_layer	1.040150935

In Table 16, we can observe that conductive loss and radiative loss in the vacuum are comparable. Given this, it would be beneficial to explore the impact of adjusting the emissivity of silver. In the next step, we will examine how changing the emissivity of silver affects the system, with the thickness of alumina set to 0.75 inches. Polished silver naturally exhibits lower emissivity compared to most materials available [46]. Initially, the emissivity of silver was 0.03, resulting in approximately 18.58 hours of time. To achieve the target time, the emissivity before vacuum should be reduced to about 0.0045, which is 85% less than the emissivity of silver. This new emissivity would decrease radiative loss in the vacuum by 84.88% and increase time by 73.58%. The time achieved with an emissivity of 0.0045 is 32.25 hours. However, such low emissivity is non-existent in the current market and academia, making it impractical for real-world applications. Let's now increase the thickness of wool to 15 inches, solely to observe the effects, while still adjusting the emissivity percentage for now. Increasing the thickness of wool to 15 inches results in only a 2.6% increase in time (33.09 hours from 32.25 hours). This change decreases q_cond_af_vac by 24.3%, but it also increases outer layer radiative loss by 25.12%.

In the upcoming analysis, we'll explore the interplay among T_alsi, T_af_vac, and T_bf_vac. Presently, we'll maintain a material with an emissivity of 0.0045, while reverting the thickness of wool to 10 inches. We acknowledge that the temperature after vacuum has a comparatively minor effect on time compared to the temperatures of Al-Si and before vacuum. Hence, we'll maintain the temperature after vacuum at a constant 525 K for the time being. In this phase of analysis, we'll investigate various values for T_alsi and T_bf_vac and their impact on target variables. It's crucial to recognize that T_bf_vac will consistently remain a certain percentage less than T_alsi. With T_alsi ranging from 850.15 to 833.15 K, to achieve the average time of 31.78 hrs, ΔT_1 (defined as $\Delta T_1 = \left(T_{alsi} - T_{bf\_vac}\right)$), should be less than 1.26 K. Smaller values of ΔT_1 results in a longer time. Likewise, a larger value of ΔT_2 (defined as $\Delta T_2 = T_{bf\_vac} - T_{af\_vac}$) also contribute to a longer time. The data is presented in Table 17 and the plot trends are shown in Graph 1 and 2.

Table 10: Shows the effect on Time varying T_alsi and T_bf_vac.

T_alsi	**T_bf_vac**	**T_af_vac**	**Time (hrs.)**	**delta T _1**	**delta_T_2**
850.15	848.874775	525	31.31751428	1.275225	323.874775
845.15	843.882275	525	31.56374592	1.267725	318.882275
840.15	838.889775	525	31.81190518	1.260225	313.889775
835.15	833.897275	525	32.06201494	1.252725	308.897275
833.15	831.900275	525	32.16261024	1.249725	306.900275
Avg	-	-	31.78355811	1.261125	314.488875

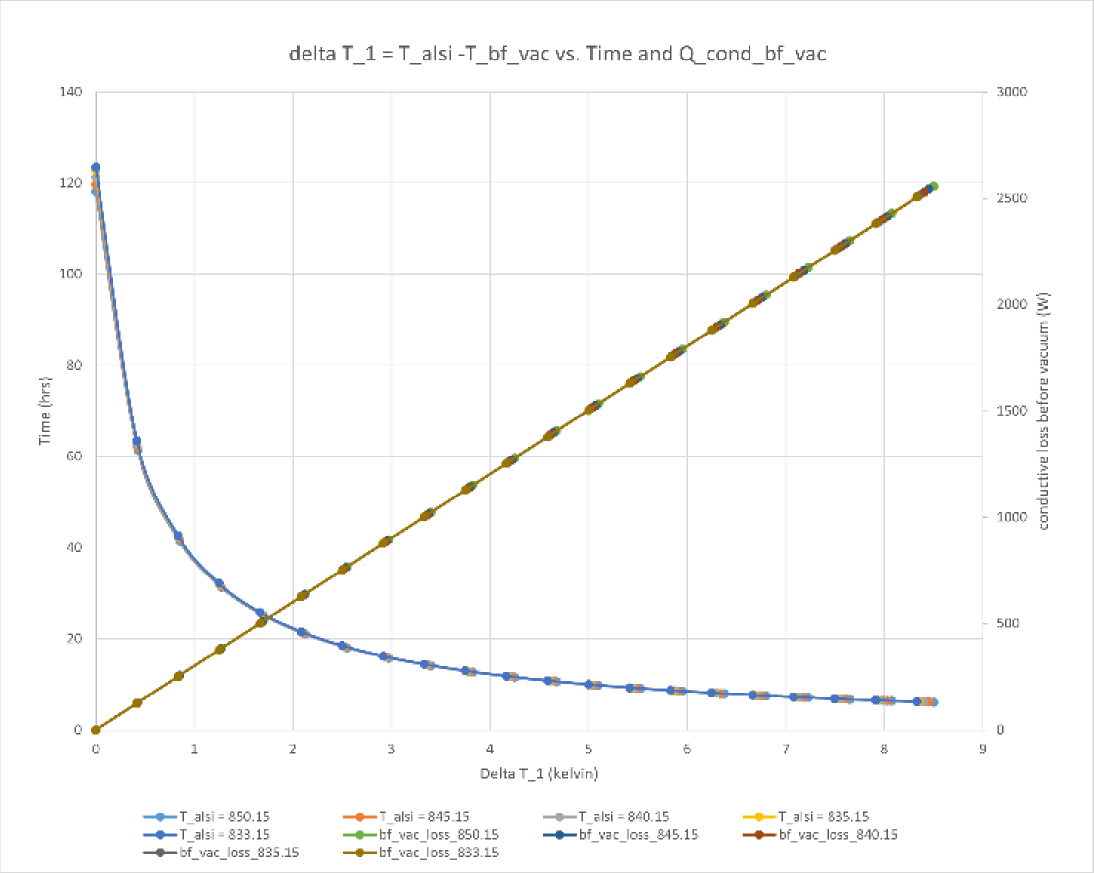

Graph 2: Illustrates the relationship between time and conductive loss before vacuum as a function of ΔT_1. The trend indicates a lower conductive loss before vacuum and longer time for a lower ΔT_1.

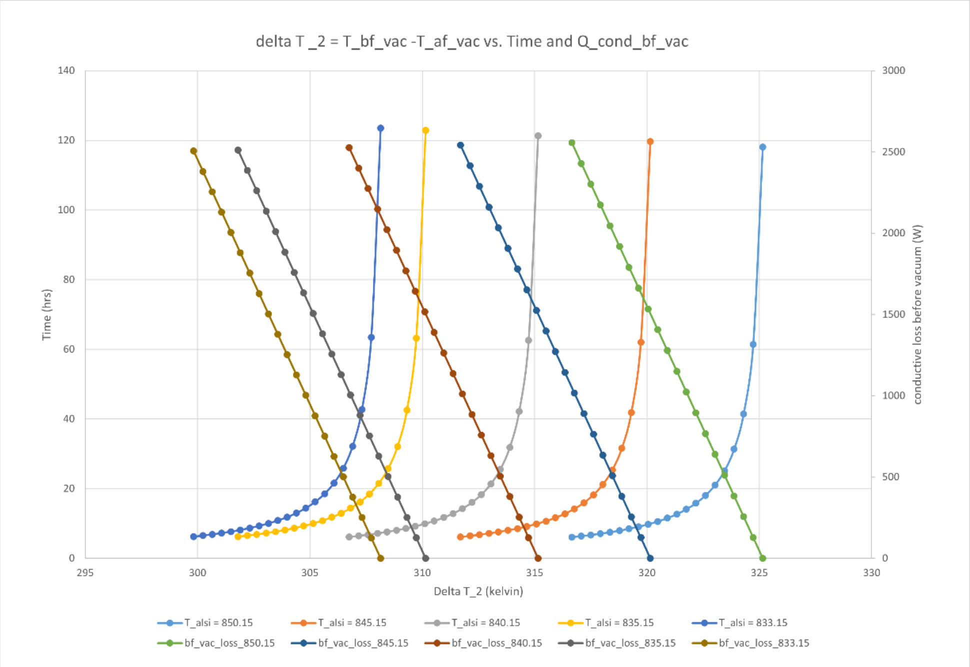

Graph 3: Illustrates the relationship between time and conductive loss before vacuum as a function of ΔT_2. The trend indicates that as ΔT_2 values increase, there is a corresponding increase in time and decrease in conductive loss before vacuum.

The necessary parameters to attain the target time are as follows: T_bf_vac should be slightly lower than T_alsi by 0.15%, and the values for Q_cond_bf_vac and Q_loss should be less than 383.514 W and 521.321 W, respectively. Mathematically presented as:

$$T_{bf\_vac} = T_{alsi} - (0.15\% * T_{alsi})$$

$$Q_{cond\_bf\_vac} < \ 383.514\ W\ ;\ Q_{loss} < 521.321\ W$$

Again, let's experiment by reducing T_af_vac by 2% to a value where T_bf_vac is 0.15% less than T_alsi, where T_alsi = 850.15. Although decreasing T_af_vac is expected to raise ΔT_2, the impact on time may not be substantial. Initially, T_af_vac is set to 525 K. Decreasing T_af_vac from 525 K to 514 K results in a time decrease from 31.31 hours to 31.13 hours, as the reduction in T_af_vac increased q_cond_af_vac from 62.33 W to 66.76 W. Additionally, increasing the thickness of wool from 10 to 15 inches resulted in an increase in time from 31.13 hours to 31.98 hours. This increase occurred because the thicker wool reduced conductive loss after vacuum from 66.76 W to 50.54 W. We further decrease T_af_vac to 472K with thickness of wool set to 15 inches. This results in conductive loss after vacuum of 36.07 W and time of 32.56 hours. We have successfully achieved the target time Case 3. At this point our target variables and input variable are as follows:

a. Target Variables:
   i. Q_loss = 501.29 W
   ii. q_cond_af_vac = 36.07 W
   iii. q_cond_bf_vac = 383.54 W
   iv. q_cond = 419.61 W
   v. q_rad_outer_layer = 11.44 W
   vi. q_rad_vacuum = 70.25 W
b. Input Variables:

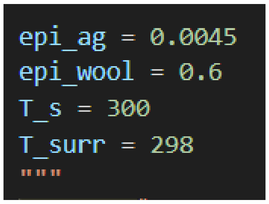

```
epi_ag = 0.0045
epi_wool = 0.6
T_s = 300
T_surr = 298
"""
```

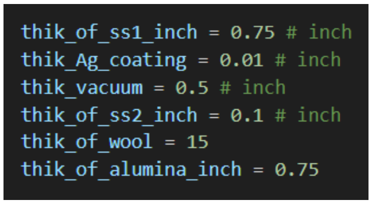

```
thik_of_ss1_inch = 0.75 # inch
thik_Ag_coating = 0.01 # inch
thik_vacuum = 0.5 # inch
thik_of_ss2_inch = 0.1 # inch
thik_of_wool = 15
thik_of_alumina_inch = 0.75
```

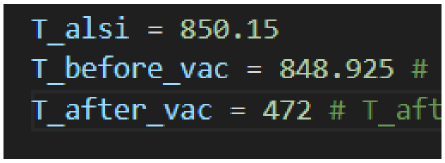

```
T_alsi = 850.15
T_before_vac = 848.925 #
T_after_vac = 472 # T_aft
```

It is essential to remember that all this is contingent on having a material coating with an emissivity of the surface is 0.0045. This value represents an 85% reduction compared to polished silver, which has an emissivity of 0.03. Let's investigate the impact of reverting the emissivity back to that of silver while keeping all other variables unchanged up to this point. The time now decreases from 32.56 to 18.226 hours as radiative loss in the vacuum increases from 70.25 W to 464.74 W.

3.4 Mathematical Analysis Summary

The analysis reveals critical insights into optimizing an advanced thermal storage system using Al-Si phase change material. We have identified key parameters affecting the system's performance, notably including temperature profiles, material thicknesses, and emissivity. Conductive heat loss, particularly before vacuum, emerges as a primary factor influencing overall heat loss, significantly impacting the system's operational time. Case 1, which does not involve a vacuum layer, successfully achieves the desired outcome with adjustments to a few parameters and an ample margin compared to Case 3. Conductive loss emerges as the primary factor influencing overall heat loss, which is mitigated effectively using kaowool insulation. It's noteworthy that the layer configuration of Case 1 is also utilized in existing real-world applications for salt as phase change material. On the other hand, Case 3 requires manipulation of numerous parameters compared to Case 1 to achieve a similar result. The primary factor contributing to overall loss is also conductive heat loss, particularly before vacuum. When the conductive heat loss before the vacuum is comparable to the radiative heat loss in the vacuum within one order of magnitude, we can achieve the desired outcome. This can be accomplished through lower values of ΔT_1(defined as $\Delta T_1 = T_{alsi} - T_{bf\_vac}$) and lower emissivity of the layer before vacuum. We observed ΔT_1 is directly proportional to conductive heat loss before vacuum. A 25% lower ΔT_1, decrease the conductivity heat loss by same amount. Similarly, the emissivity of layer before the vacuum (in this study, a silver coating) is also directly proportional to radiative loss in the vacuum. A 10% decrease in emissivity decreases radiative loss in vacuum by 9.988%. The calculation suggests that T_{bf_vac} less than T_{alsi} by 0.15%, with emissivity of 0.0054, and kaowool thickness of 10 in" will yield the desired operational time of 32.04 hours. These four parameters have the most significant effect on heat loss.

While our findings present promising avenues for achieving target operational times for Case 3, practical implementation considerations and material availability remain essential factors in realizing these advancements. The performance of Case 3 is heavily reliant on achieving an extremely low emissivity value (0.0045), a parameter that is currently unattainable in real-world applications [46]. Moreover, Case 3 fails to offer significant advantages over Case 1; instead, it introduces additional avenues for heat loss. The mechanical infrastructure required to maintain the vacuum layer further complicates the system, requiring constant monitoring to ensure the vacuum state. Implementing and managing such a system for a single household entails considerable effort and complexity. Based on these considerations, it is reasonable to speculate that Case 3 would incur significantly higher costs compared to Case 1.

A more comprehensive study of temperature profiles can be conducted using software such as COMSOL and ANSYS, leading to more accurate estimations of heat loss. However, it's important to note that while this analysis assumes a steady-state condition, real-world applications of such systems are often dynamic and non-steady-state. Therefore, a deeper understanding of the temperature profile is essential for practical implementation.

CHAPTER 4: CONCLUSION

In this study, we examine the different subsystems in a benchtop prototype of latent heat system. Additionally, we perform the first order optimizations of input parameters for thermal storage container aimed at maintaining the temperature of Al-Si at 577°C for 24-32 hours.

The experimental and theoretical investigations shed light on the challenges and potential avenues for optimizing an advanced thermal storage system utilizing Al-Si phase change material. The bench-top experimental setup, while not entirely successful, provided valuable insights into the feasibility of small-scale thermal energy storage using eutectic Al-Si alloy. It highlighted the limitations of thermoelectric generators (TEGs) in converting thermal energy into electrical energy, as well as the unsuitability of 304 stainless steel for long-term containment of molten Al-Si. Additionally, the inefficient heating setup highlighted the importance of thermal continuity and uniform heating in such systems.

On the theoretical front, the analysis emphasized the critical role of parameters such as temperature profiles, material thicknesses, and emissivity in influencing system performance. Case 1 demonstrated that adjustments to a few parameters, particularly the use of kaowool insulation, can effectively mitigate conductive heat loss and achieve desired outcomes with a significant margin compared to Case 3. Conversely Case 3's reliance on an extremely low emissivity value poses practical challenges and fails to offer substantial advantages over Case 1, thereby complicating the system and increasing operational complexity. A comprehensive study of temperature profiles using advanced software tools like COMSOL and ANSYS can enhance the accuracy of heat loss estimations. In addition, the non-steady-state nature of real-world applications necessitates a deeper understanding of temperature profiles for practical implementation.

LHS is multidimensional and multidisciplinary system and while our study doesn’t provide a rigid solution to the problems of thermal energy storage, the experimental and theoretical approaches provide valuable insight into the first order challenges to these types of systems. Compared to Case 3, case 1 emerges as a more viable option for optimizing thermal storage tanks using Al-Si as phase change materials, offering realistic solution with fewer complexities. Our study does not account for how corrosion will affect the system. Another significant aspect we have overlooked is the heat loss during the transfer of thermal energy. Given that we maintain Al-Si at the phase change temperature for 32 hours, it is important to recognize that the actual duration available for producing output power may be less due to losses during thermal energy transfer.

APPENDIX A

A1. Supplement Information

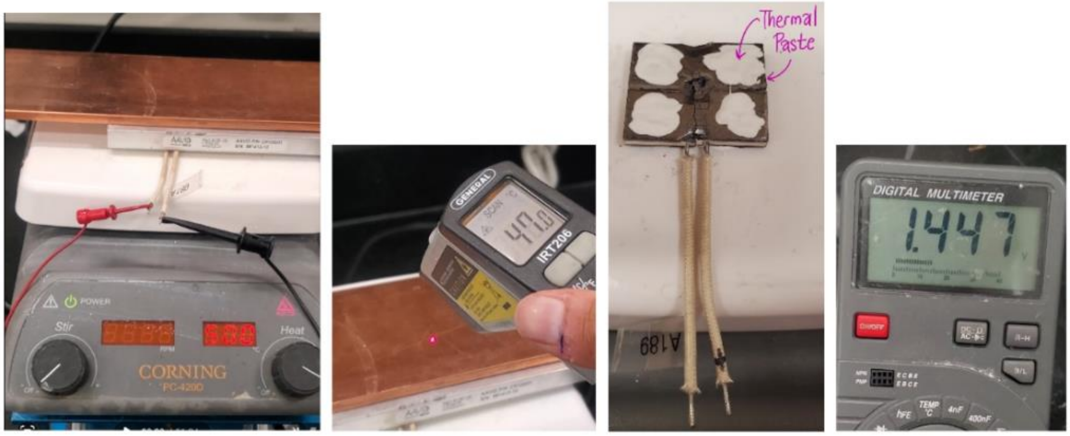

Figure 17: The heating plate was set to 500°C, while a water heat exchanger with an ice bath circulating through it was employed to cool down the other side of the TEG. Using this setup, a voltage output of 1.45 V was measured on the voltmeter.

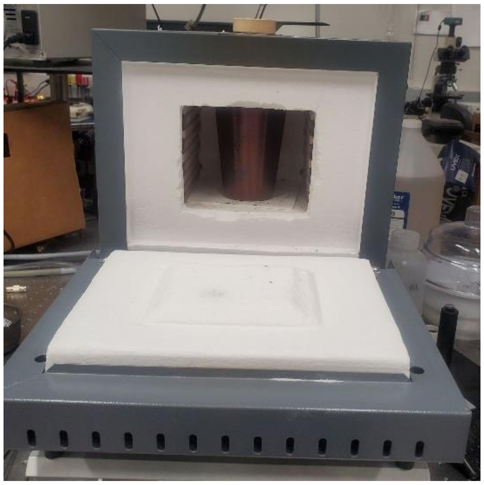

Figure 18: The image depicts a 12 oz. 304 stainless-steel cup containing 300 g of Al-Si inside a muffled furnace.

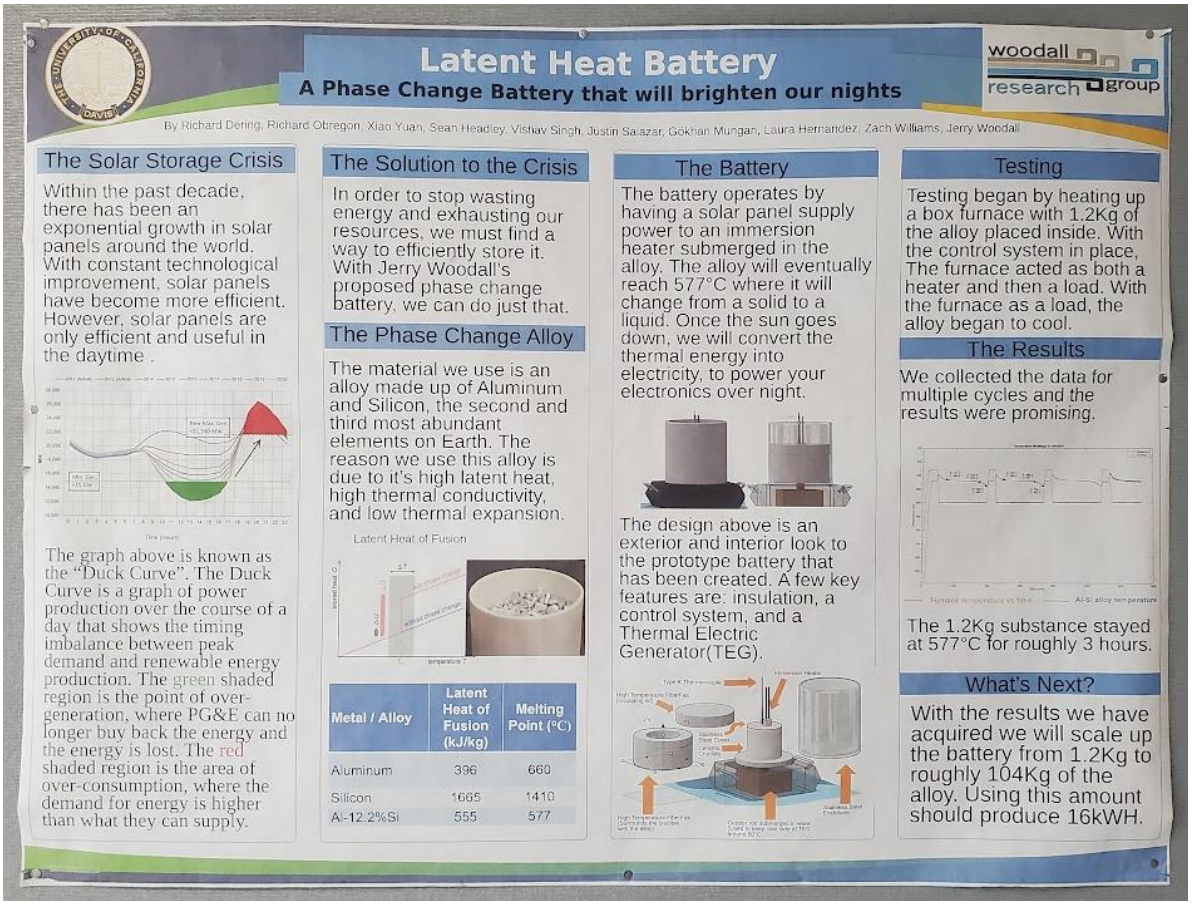

Latent Heat Battery

A Phase Change Battery that will brighten our nights

By Richard Dering, Richard Obregon, Xiao Yuan, Sean Headley, Vishav Singh, Justin Salazar, Gökhan Mungan, Laura Hernandez, Zach Williams, Jerry Woodall

The Solar Storage Crisis

Within the past decade, there has been an exponential growth in solar panels around the world. With constant technological improvement, solar panels have become more efficient. However, solar panels are only efficient and useful in the daytime .

The graph above is known as the “Duck Curve”. The Duck Curve is a graph of power production over the course of a day that shows the timing imbalance between peak demand and renewable energy production. The green shaded region is the point of over-generation, where PG&E can no longer buy back the energy and the energy is lost. The red shaded region is the area of over-consumption, where the demand for energy is higher than what they can supply.

The Solution to the Crisis

In order to stop wasting energy and exhausting our resources, we must find a way to efficiently store it. With Jerry Woodall's proposed phase change battery, we can do just that.

The Phase Change Alloy

The material we use is an alloy made up of Aluminum and Silicon, the second and third most abundant elements on Earth. The reason we use this alloy is due to it's high latent heat, high thermal conductivity, and low thermal expansion.

Metal / Alloy	Latent Heat of Fusion (kJ/kg)	Melting Point (°C)
Aluminum	396	660
Silicon	1665	1410
Al-12.2%Si	555	577

The Battery

The battery operates by having a solar panel supply power to an immersion heater submerged in the alloy. The alloy will eventually reach 577°C where it will change from a solid to a liquid. Once the sun goes down, we will convert the thermal energy into electricity, to power your electronics over night.

The design above is an exterior and interior look to the prototype battery that has been created. A few key features are: insulation, a control system, and a Thermal Electric Generator(TEG).

Testing

Testing began by heating up a box furnace with 1.2Kg of the alloy placed inside. With the control system in place, The furnace acted as both a heater and then a load. With the furnace as a load, the alloy began to cool.

The Results

We collected the data for multiple cycles and the results were promising.

The 1.2Kg substance stayed at 577°C for roughly 3 hours.

What's Next?

With the results we have acquired we will scale up the battery from 1.2Kg to roughly 104Kg of the alloy. Using this amount should produce 16kWH.

Figure 19: The image depicts a 12 oz. 304 stainless-steel cup containing 300 g of Al-Si inside a muffled furnace.

Figure 20: The above images depict various stages of the stainless-steel cup during the testing experiment. Pictures a. and b. show the cup in its unused state, while c. illustrates its condition after being removed from the furnace due to leakage. Images d. and e. reveal leaked Al-Si and the subsequent dissolution of the stainless-steel cup. Following the dissolution process using Sodium Hydroxide (NaOH), corrosion is evident, as shown in pictures f., g., and h., with a notable build-up observed at the bottom of the cup in picture f. Additionally, pictures i. and j. display cut-out pieces of the unused and experimented cups, respectively, which were further analyzed under SEM. Energy-Dispersive X-ray Spectroscopy (EDS), could be conducted to examine the elemental composition of materials, particularly on the bottom and sides of the cup. EDS was not performed for this study.

APPENDIX B

B1. Formulae

$$\text{average power year} = \frac{\text{annula elec demand}}{\text{hrs per year}} * \text{watts per kW [Watts]}$$

$$\text{annual lhe} = \text{average power year} * \text{hrs per year} * \text{seconds per year [joules/year]}$$

$$\text{total lhe} = \frac{(\text{annual lhe})}{\text{no of phase change per year}} \text{ [Joules]}$$

$$\text{mass of alsi} = \frac{(\text{total lhe})}{\text{lhv alsi}} \text{ [kg]}$$

$$\text{volume of alsi} = \frac{(\text{mass of alsi})}{\text{rho alsi}} \text{ [m}^3\text{]}$$

$$\text{headspace volume} = 1 + \frac{(\text{headspace value})}{100} \text{ [unitless]}$$

$$\text{volume of container} = \text{volume of alsi} * \text{headspace volume [m}^3\text{]}$$

$$\text{volume of alsi} = \frac{\text{volume of container}}{\text{headspace volume}} \text{ [m}^3\text{]}$$

$$\text{surface area} = 2\pi rh + 2\pi r^2 \text{ [m}^2\text{]}$$

$$\text{volume} = \pi r^2 h \text{ (r =r\_inner, [m}^2\text{])}$$

B2. Constants, Variables, and functions

Stefan Boltzmann constant (stef_boltz) = $5.67 * 10^{-8}\ \frac{\mathrm{W}}{\mathrm{m^2\ K}}$

Table 11: Unit conversion values used in the analysis.

Name	Value	Units
hrs_per_year	8760	hrs/year
month_per_year	12	month/year
hrs_per_day	24	hrs/day
days_per_year	365	day/year
sec_per_hrs	3600	sec/hrs
inch_to_meters	0.0254	in”/m
joules_per_kwh	$3.6 * 10^6$	J/kWh
watts_per_kW	1000	W/kW
BTU_k_units_to_SIunits	0.1441314	-

Table 12: Eutectic Al-12wt%Si properties.

Name	Code name	Value	Units
Density	rho_Al-Si	2700	kg/m^3
Latent Heat Value	lhv_Al-Si	470000	J/kg
Phase Change Temperature	pct_Al-Si	850.15	K

Table 13: Thermal conductivity of materials [W/m-K].

Material	Code name	Value
304 Stainless Steel	k_304SS	16.2
Alumina (Al_2O_3)	k_al2o3	30.0
Silver	k_ag	428
Kaowool	k_wool	0.54 * BTU_k_units_to_SIunits = 0.077830956

Table 14: Emissivity [unitless].

Material	**Code name**	**Value**
Polished Silver	epi_ag	0.03 (here)
Kaowool	epi_wool	0.6
304 Stainless Steel	epi_304SS	0.757 (here)

Table 15: Initial temperature at layer boundaries [kelvin].

Temperature	**Value [K]**
T_surr	293
T_alsi	850.15
T_s	300
T_before_vac	825
T_after_vac	T_before_vac – T_s

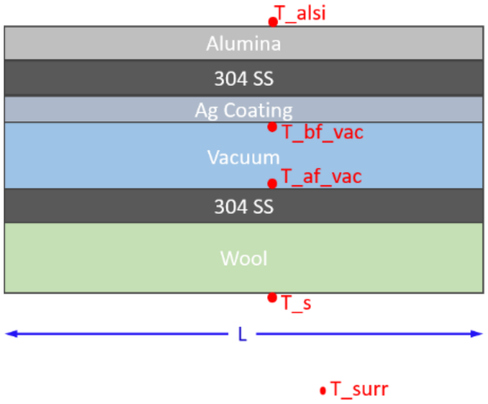

Table 16: Initial thickness of the layers [in"].

Layer name	**Code name (inch)**	**Value [in”]**	**Code name (meters)**
Alumina	thik_of_alumina_inch	0.1	thik_alum_m
304 Stainless Steel 1	thik_of_ss1_inch	0.1	thik_ss1_m
Silver Coating	thik_Ag_coating	0.01	thik_Ag_coat_m
Vacuum	thik_alum_m	0.5	thik_vac_m
304 Stainless Steel 2	thik_of_ss2_inch	0.1	thik_ss2_m
Kaowool	thik_of_wool	1	thik_wool_m

B3. Phase 1 Data

Table 17: Shows the respective average power per year, annual latent heat energy, total latent heat energy, mass, and volume calculated based on the annual electricity consumption per household.

	Annual electricity consumption (kWh/year)**	Average power year (kW)	Annual latent heat (Joules/year)	Total latent heat (Joules)	Mass of Al-Si (kg)	Volume of Al-Si (m^3)
maximum	14302	1632.648402	51487200000	58775342.47	125.0539201	0.046316267
average	10632	1213.69863	38275200000	43693150.68	92.96415039	0.034431167
minimum	6369	727.0547945	22928400000	26173972.6	55.68930341	0.020625668

**Annual electricity consumption for a U.S. residential utility customer (per household) (kWh/year)

Below we have the calculated target variables for different headspaces and cases for the maximum annual electricity consumption per household.

Table 18: Shows the time calculated for different headspaces and cases for maximum annual electricity consumption for a household.

time (hrs.)					
headspace	**0**	**1**	**5**	**10**	**20**
case 0	0.0148	0.0147	0.0144	0.0139	0.0131
case 1	18.3937	18.2771	17.8287	17.3059	16.3680
case 2	0.2847	0.2829	0.2757	0.2674	0.2524
case 3	0.3207	0.3186	0.3105	0.3011	0.2842

Table 19: Shows the total loss calculated for different headspaces and cases for maximum annual electricity consumption for a household.

Q_loss (Watts)					
headspace	**0**	**1**	**5**	**10**	**20**
case 0	1100703.92	1107975.92	1136825.66	1172374.18	1241886.56
case 1	887.61	893.28	915.74	943.41	997.46
case 2	57338.77	57716.90	59217.00	61065.36	64679.54
case 3	50913.38	51249.56	52583.24	54226.59	57439.98

Table 20: Conductive loss after vacuum varying cases and headspaces.

conductive loss after vacuum					
headspace	**0**	**1**	**5**	**10**	**20**
case 2	383.2379	385.6056	394.9934	406.5496	429.1123
case 3	383.6664	386.0355	395.4289	406.9919	429.5676

Table 21: Conductive loss before vacuum.

conductive loss before vacuum					
headspace	**0**	**1**	**5**	**10**	**20**
case 2	50317.766	50650.199	51969.041	53594.112	56771.813
case 3	50195.812	50527.435	51843.062	53464.172	56634.125

Table 22: Total conductive loss varying headspaces and cases.

conductivity loss					
headspace	**0**	**1**	**5**	**10**	**20**
case 0	1100688.6	1107960.5	1136809.9	1172357.9	1241869.3
case 1	873.94218	879.52146	901.64931	928.90138	982.14917

Table 23: Radiative loss in the vacuum.

radiative loss in the vacuum					
headspace	**0**	**1**	**5**	**10**	**20**
case 2	6623.1708	6666.4093	6837.9292	7049.2375	7462.3209
case 3	319.2888	321.3848	329.6997	339.9445	359.9745

Table 24: Radiative loss from the outer layer.

radiative loss outer layer					
headspace	**0**	**1**	**5**	**10**	**20**
case 0	15.3018	15.4023	15.8012	16.2926	17.2535
case 1	13.6708	13.7556	14.0919	14.5060	15.3144
case 2	14.5964	14.6843	15.0327	15.4614	16.2980
case 3	14.6118	14.6997	15.0484	15.4773	16.3144

Table 25: Surface area to volume ratio.

SAV ratio					
headspace	**0**	**1**	**5**	**10**	**20**
case 0	15.9547	20.5566	20.4707	20.1389	19.7496
case 1	18.7597	15.9001	15.6887	15.4394	14.9838
case 2	18.7597	18.6861	18.4020	18.0680	17.4613
case 3	20.5267	20.4409	20.1100	19.7216	19.0179

B4. Phase 2, Part 1

Table 26: For case 1

percent_change	input_variable	initial value	q_cond %	q_rad_outer_layer %	Q_loss %	time %
-0.5	epi_wool	0.6	0	-0.5	-0.007694282	0.007694874
-2	T_alsi (K)	850 (ideal case)	-3.090611651	0	-3.043051579	3.138559565
2	T_surr (K)	293	0	-83.22897096	-1.280774274	1.297390923
2	T_s (K)	300	-1.090611651	-86.1454338	-0.251825742	0.252461505
-20	thik_alum_m	0.00254	-0.230568582	-0.222524242	-0.230444791	0.230977066
-20	thik_ss1_m	0.00254	-0.225837249	-0.222524242	-0.225786266	0.226297214
20	thik_wool_m	0.0254	-15.7141475	2.225242419	-15.43808607	18.2565476

Table 27: For case 3

% change*	ip_var		q_cond_af_vac %	q_cond_bf_vac %	q_cond %	q_rad_vac %	q_rad_out_layer %	Q_loss %	time %
-0.5	epi_wool	0.6	0	0	0	0	-0.5	-0.00014309	0.00014309
-0.5	epi_ag	0.03	0	0	0	-0.495582729	0	-0.00310733	0.003107427
-2	T_alsi (K)	850.15	0	-67.606361	-67.09460	0	0	-66.65471492	199.8924728
2	T_surr (K)	293	0	0	0	0	-83.22897096	-0.023818608	0.023824283
-2	T_s (K)	300	2.66667	0	0.02018	0	-86.1454338	-0.004599763	0.004599974
-2	T_af_vac (K)	525	-4.66667	0	-0.035325	1.522827188	0	-0.025545388	0.025551916
0.5	T_bf_vac (K)	825	0	-16.40159	-16.27743	2.410322546	0	-16.15560402	19.26855556
20	thik_alum_m	0.00254	0.22028	-6.39975	-6.34964	0.249914276	0.208381417	-6.306385105	6.730858995
20	thik_ss1_m	0.00254	0.22028	-11.34775	-11.26018	0.249914276	0.208381417	-11.1847349	12.59325735
-20	thik_vac_m	0.0127	-1.10143	0	-0.00833	-0.010446975	-1.041907086	-0.008646533	0.00864728
-20	thik_ss2_m	0.00254	-0.21004	0	-0.00158	-0.002070082	-0.208381417	-0.001652169	0.001652196
20	thik_wool_m	0.0254	-15.77868	0	-0.11943	0	2.083814173	-0.118060275	0.118199823

*Positive values are percent increase and negative values are percent decrease.

*We take the percent change that will increase the time.

B5. Phase 2, Part 2

Table 28: Shoes the relation between thickness of wool, time, and total loss for case 1.

thick_wool (in")	time (hrs.)	Q_loss (W)	poly. (time(hrs.))	power(Q_loss(W))	time discrepancy	Q_loss discrepancy
1.00000	16.79845	971.90395	16.83831	963.02954	0.23725	0.91310
1.01000	16.95599	962.87386	16.99250	954.64329	0.21529	0.85479
1.10000	18.36581	888.96082	18.37452	885.63636	0.04744	0.37397
1.11000	18.52157	881.48508	18.52745	878.61925	0.03175	0.32511
1.20000	19.91549	819.78837	19.89808	820.42577	0.08741	0.07775
1.50000	24.46173	667.42972	24.39281	674.30347	0.28173	1.02988
2.00000	31.71438	514.79749	31.63092	523.64172	0.26318	1.71800
2.50000	38.59135	423.06076	38.55262	430.37828	0.10035	1.72966
3.00000	45.12308	361.82117	45.15792	366.64860	0.07722	1.33420
3.50000	51.33631	318.02996	51.44682	320.18708	0.21528	0.67827
4.00000	57.25465	285.15561	57.41933	284.72715	0.28762	0.15025
4.50000	62.89906	259.56642	63.07543	256.72361	0.28039	1.09521
5.00000	68.28826	239.08186	68.41513	234.01569	0.18579	2.11901
5.50000	73.43902	222.31348	73.43843	215.20919	0.00080	3.19562
6.00000	78.36646	208.33511	78.14533	199.36305	0.28217	4.30655
average	-	-	-	-	0.14483	1.01359

B6. Calculation in Python

Table 29: Important functions and their application in the code.

Function Name	**Description**
filename: function.py	
vol_of_container	Calculates volume of the container given the volume of Al-Si and the headspace.
check_vacuum_layer	Checks if the lowercase version of the layer name contains vacuum.
find_last_layer	Checks the layer data in reverse, make sure that the last layer is not vacuum, if it is not vacuum, assigns that layer as the last layer of the layer data.
find_layers_around_vacuum	Finds the name of the layer before and after vacuum layer.
calculate_outer_radius	Calculates and stores the radius for each layer.
conductive_heat_loss	Calculated conductive loss.
assign_emissivity	Assigns emissivity with layer name.
get_emissivity	Gets emissivity of necessary layers for the given case.
get_outer_layer_q_rad	Calculates radiative loss of the outer most layer.
get_vacuum_layer_q_rad	Calculates radiative loss of the vacuum layer.
filename: main_i.py	
cal_case	This function takes input of headspace list and case_choice list, calculates all the losses, surface area to volume ratio, and time for each case in the list for all headspace percentages.

Python codes are available in the following links:

- 🗀 anshu_thesis_2024
  - readme.md
  - 🗀 experimental_calc
    - 060623.py
  - 🗀 Phase 1
    - constant.py
    - function.py
    - main_i.py
    - pwr_engy.py
  - 🗀 Phase 2
    - constant.py
    - exc.py
    - function.py
    - percent_array.py
    - sensitivity.py
  - 🗀 T_alsi_n_T_bf_vac
    - constant.py
    - function.py
    - percent_array.py

sensitivity_analysis_final.py

CHAPTER 5: REFERENCE

[1] Thermal Energy Storage, European Association for Storage Energy, Brussels, 2023

[2] Ho, Clifford K., and Andrea Ambrosini. Thermal Energy Storage Technologies, Sandia National Laboratories. https://www.sandia.gov/ess-ssl/wp-content/uploads/2020/12/ESHB_Ch12_Thermal_Ho.pdf

[3] Zalba, B., Marin, J. M., Cabeza, L.F., & Mehling, H. (2003). Review on thermal energy storage with phase change: Materials, Heat Transfer Analysis and Application. Applied Thermal Engineering, 23(3), 251-283.

[4] The History of Solar, U.S. Department of Energy, Energy Efficiency and Renewable Energy https://www1.eere.energy.gov/solar/pdfs/solar_timeline.pdf

[5] Nevada Solar One CSP Project, NREL Transforming Energy. https://solarpaces.nrel.gov/project/nevada-solar-one

[6] Crescent Dune Solar Energy Project CSP Project, NREL Transforming Energy. https://solarpaces.nrel.gov/project/crescent-dunes-solar-energy-project

[7] Thermal Storage System Concentrating Solar-Thermal Power Basics, Office of Energy Efficiency & Renewable Energy https://www.energy.gov/eere/solar/thermal-storage-system-concentrating-solar-thermal-power-basics

[8] Nevada Solar One, Wikipedia. https://en.wikipedia.org/wiki/Nevada_Solar_One

[9] Laurent, Steven J. Thermocline Thermal Storage Test for Large-Scale Solar Thermal Power Plants. United States: N. p., 2000.Web.

[10] Solar Two Demonstrates clean power for the future, NREL Transforming Energy. https://www.nrel.gov/docs/legosti/fy97/22835.pdf

[11] The Solar Project, Wikipedia. https://en.wikipedia.org/wiki/The_Solar_Project

[12] Crescent Dune Solar Energy Project CSP Project, NREL Transforming Energy. https://solarpaces.nrel.gov/project/crescent-dunes-solar-energy-project

[13] Solar plant near Tonopah producing power for NV Energy after stop during backruptcy, NEWSNOW.com.

[14] Crescent Dunes Solar Energy Projects, Wikipedia https://en.wikipedia.org/wiki/Crescent_Dunes_Solar_Energy_Project

[15] Solana Generating Station CSP Project, NREL Transforming Energy, https://solarpaces.nrel.gov/project/solana-generating-station

[16] Concentrating Solar Power Projects in United States, NREL Transforming Energy. https://solarpaces.nrel.gov/by-country/US

[17] Bauer, Thomas, et al. Molten Salt Storage for Power Generation. 11 Feb. 2021.

[18] Jonathan E. Rea, Christopher J. Oshman, Abhishek Singh, Jeff Alleman, Greg Buchholz, Philip A. Parilla, Jesse M. Adamczyk, Helena-Nikolai Fujishin, Brenden R. Ortiz, Tara Braden, Erik Bensen, Robert T. Bell, Nathan P. Siegel, David S. Ginley, Eric S. Toberer, Prototype latent heat storage system with aluminum-silicon as a phase change material and a Stirling engine for electricity generation, Energy Conversion and Management,Volume 199, 2019. https://doi.org/10.1016/j.enconman.2019.111992

[19] Jonathan E. Rea, Christopher J. Oshman, Abhishek Singh, Jeff Alleman, Philip A. Parilla, Corey L. Hardin, Michele L. Olsen, Nathan P. Siegel, David S. Ginley, Eric S. Toberer, Experimental demonstration of a dispatchable latent heat storage system with aluminum-

silicon as a phase change material, Applied Energy,Volume 230, 2018. https://doi.org/10.1016/j.apenergy.2018.09.017

[20] Abdallah Dindi, Nicolas Lopez Ferber, Daniel Gloss, Erik Rilby, Nicolas Calvet, Compatibility of an Aluminium-Silicon metal alloy-based phase change material with coated stainless-steel containers, Journal of Energy Storage, 2020. https://doi.org/10.1016/j.est.2020.101961

[21] Xian-man ZHANG, Wei-ping CHEN, Review on corrosion-wear resistance performance of materials in molten aluminum and its alloys,Transactions of Nonferrous Metals Society of China,Volume 25, Issue 6, 2015. https://doi.org/10.1016/S1003-6326(15)63777-3

[22] Haoxin Xu, Fabio Dal Magro, Najim Sadiki, Jean-Marie Mancaux, Xavier Py, Alessandro Romagnoli, Compatibility study between aluminium alloys and alternative recycled ceramics for thermal energy storage applications, Applied Energy, 2018. https://doi.org/10.1016/j.apenergy.2018.03.021

[23] Ryo Fukahori, Takahiro Nomura, Chunyu Zhu, Nan Sheng, Noriyuki Okinaka, Tomohiro Akiyama, Thermal analysis of Al–Si alloys as high-temperature phase-change material and their corrosion properties with ceramic materials, Applied Energy, Volume 163, 2016, Pages 1-8, ISSN 0306-2619, https://doi.org/10.1016/j.apenergy.2015.10.164.

[24] Dering, R., Obregon, R., Yuan, X., Headley, S., Singh, V., Salazar, J., Mungan, G., Hernandez, L., Williams, Z., & Woodall, J. Latent Heat Battery: A phase change battery that will brighten our nights.

[25] Hi-Density Cartiridge Heater Specification and Tolerance, Tempco.

[26] Medveď, Dušan, et al. “Latent Heat Storage Systems.” University of West Bohemia, 31 Dec. 2009, https://core.ac.uk/download/pdf/295581073.pdf

[29] N. Gokon, S. Nakamura, T. Yamaguchi, T. Kodama,Cyclic Properties of Thermal Storage/Discharge for Al-Si Alloy in Vacuum for Solar Thermochemical Fuel Production, Energy Procedia, Volume 69,2015,Pages 1759-1769, https://www.sciencedirect.com/science/article/pii/S1876610215004518.

[30] Samuel Reed, Heber Sugo, Erich Kisi,High temperature thermal storage materials with high energy density and conductivity, Solar Energy, Volume 163,2018,Pages 307-314, https://www.sciencedirect.com/science/article/pii/S0038092X18301221.

[31] Zhengyun Wang, Hui Wang, Mei Yang, Wenwen Sun, Guangfu Yin, Qinyong Zhang, Zhifeng Ren,Thermal reliability of Al-Si eutectic alloy for thermal energy storage, Materials Research Bulletin, Volume 95, 2017, https://www.sciencedirect.com/science/article/pii/S0025540817319487.

[32] A. Inés Fernández, Camila Barreneche, Martin Belusko, Mercè Segarra, Frank Bruno, Luisa F. Cabeza, Considerations for the use of metal alloys as phase change materials for high temperature applications, Solar Energy Materials and Solar Cells, 2017. https://www.sciencedirect.com/science/article/pii/S0927024817303707

[33] Ming Liu, Ehsan Shamil Omaraa, Jia Qi, Pegah Haseli, Jumal Ibrahim, Dmitry Sergeev, Michael Müller, Frank Bruno, Peter Majewski, Review and characterization of high-temperature phase change material candidates between 500 C and 700°C, Renewable and Sustainable Energy Reviews, 2021. https://www.sciencedirect.com/science/article/pii/S1364032121008066

[34] Ryo Fukahori, Takahiro Nomura, Chunyu Zhu, Nan Sheng, Noriyuki Okinaka, Tomohiro Akiyama, Thermal analysis of Al–Si alloys as high-temperature phase-change material

and their corrosion properties with ceramic materials, Applied Energy, 2016. https://www.sciencedirect.com/science/article/pii/S0306261915014063

[35] Thiago Torres Martins Rocha, Paulo Vinicius Trevizoli, Raphael Nunes de Oliveira, A timeline of the phase-change problem for latent thermal energy storage systems: A review of theoretical approaches from the 1970′s to 2022, Solar Energy, 2023. https://www.sciencedirect.com/science/article/pii/S0038092X22009069

[36] Haojie Zhang, Xiaoguang Zhang, Dean Pan, Yonghong Ai, Yousheng Chen, Preparation and application of high-temperature composite phase change materials, Journal of Energy Storage, Volume 68, 2023, https://www.sciencedirect.com/science/article/pii/S2352152X23010666

[37] Abdallah Dindi, Nicolas Lopez Ferber, Daniel Gloss, Erik Rilby, Nicolas Calvet, Compatibility of an Aluminium-Silicon metal alloy-based phase change material with coated stainless-steel containers, Journal of Energy Storage, Volume 32, 2020, https://www.sciencedirect.com/science/article/pii/S2352152X20317977

[38] S Rawson, Anthony & Villada, Carolina & Kolbe, Matthias & Stahl, Veronika & Kargl, Florian. (2021). Suitability of Aluminium Copper Silicon eutectic as a phase change material for thermal storage applications: Thermophysical properties and compatibility. Energy Storage. 4. 10.1002/est2.299.

[39] Arthur K.A. Araújo, Gabriel I. Medina T., Analysis of the effects of climatic conditions, loading level and operating temperature on the heat losses of two-tank thermal storage systems in CSP, Solar Energy, Volume 176, 2018, Pages 358-369, https://www.sciencedirect.com/science/article/pii/S0038092X18310004

[40] Cristina Prieto, Javier Ruiz-Cabañas, Virginia Madina, A. Inés Fernández, Luisa F. Cabeza, Lessons learned from corrosion of materials with molten salts during molten salt tank preheating, Solar Energy Materials and Solar Cells, Volume 247, 2022, https://www.sciencedirect.com/science/article/pii/S0927024822003610

[41] Qing Gong, Andrea Hanke, Fiona Kessel, Alexander Bonk, Thomas Bauer, Wenjin Ding, Molten chloride salt technology for next-generation CSP plants: Selection of cold tank structural material utilizing corrosion control at 500 °C, Solar Energy Materials and Solar Cells, Volume 253, 2023, https://www.sciencedirect.com/science/article/pii/S0927024823000545

[42] Alnaimat, F., Rashid, Y. Thermal Energy Storage in Solar Power Plants: A Review of the Materials, Associated Limitations, and Proposed Solutions. Energies **2019**, 12, 4164. https://doi.org/10.3390/en12214164

[43] Sensitivity Analysis Definition, Investopedia. https://www.investopedia.com/terms/s/sensitivityanalysis.asp

[44] Advanced Thermal Storage System with Novel Molten Salt, NREL https://www.nrel.gov/docs/fy13osti/58595.pdf

[45] How much electricity does an American home use? U.S. Energy Information Administration https://www.eia.gov/tools/faqs/faq.php?id=97&t=3

[46] Table of Emissivity of Various Surfaces, Transmetra https://www.transmetra.ch/images/transmetra_pdf/publikationen_literatur/pyrometrie-thermografie/emissivity_table.pdf

[47] Phase Change Materials Thermal Energy Storage Design Guide, Version 2011, Phase Change Material Products https://www.pcmproducts.net/files/design_manual.pdf

[48] Bergman, T. L., and Frank P. Incropera. Fundamentals of Heat and Mass Transfer. Seventh edition. Wiley, 2011.
[49] View Factor, Thermal Radiation in Heat Transfer, Ansys https://courses.ansys.com/wp-content/uploads/2020/05/Lesson-2-View-factors.pdf
[50] Cengel, Y., Ghajar, A. (2015). Title of the book (5th ed.). McGraw-Hill Education. Chapter 13: Radiation Heat Transfer. Heat and Mass Transfer (pp. 791-810).

Material Reference [M]

[M1] TEG specification
[M2] Grainger J type Thermocouple
[M3] Grainger Heater
[M4] Tempco Cartridge Heater
[M5] Stainless Steel Container
[M6] 3000W Transformer
[M7] Aluminum Oxide